Geochimica et Cosmochimica Acta 422 (2026) 617–633

Contents lists available at ScienceDirect

Geochimica et Cosmochimica Acta

journal homepage: www.elsevier.com/locate/gca

Late Cretaceous cerium anomalies and globally distinctive redox responses before, during and after Oceanic Anoxic Event 2☆

Cheng Cao [a,b,*], Xiao-Ming Liu [c], Jeremy D. Owens [d], Hugh C. Jenkyns [e]

[a] International Center for Isotope Effects Research, Nanjing University, Nanjing 210023, China
[b] Frontiers Science Center for Critical Earth Material Cycling, Ministry of Education, State Key Laboratory of Critical Earth Material Cycling and Mineral Deposits, School of Earth Sciences and Engineering, Nanjing University, Nanjing 210023, China
[c] University of North Carolina at Chapel Hill, Department of Marine, Earth and Environmental Sciences, Chapel Hill, NC, USA
[d] Department of Earth, Ocean and Atmospheric Science & National High Magnet Field Laboratory, Florida State University, Tallahassee, FL 32306, USA
[e] Department of Earth Sciences, University of Oxford, South Parks Road OX1 3AN, UK

ARTICLE INFO

Co-Guest Editor: Ricardo Arevalo Jr.

ABSTRACT

Mesozoic oceanic anoxic events (OAEs) reflect major disruptions in the carbon cycle, characterized by elevated CO_2 in the oceans and atmosphere, global warming, and widespread organic-carbon burial. As the quintessential OAE, Oceanic Anoxic Event 2 (OAE 2, ~94 Ma) serves as a critical benchmark for investigating the extent of oceanic anoxia associated with carbon-cycle dynamics. This study uses Ce anomalies in marine carbonates to assess spatially variable redox changes during OAE 2 (Cenomanian–Turonian). The temporal evolution of deoxygenation and the triggering mechanism has been most extensively studied in the European pelagic shelf sea, proto-North Atlantic and Western Interior Seaway. The redox response in the Indian Ocean to this event remains less well-constrained. Data from seven sections—Eastbourne (UK), Raia del Pedale (Italy), and Clot Chevalier (France) in the Tethyan continental margins, plus ODP/IODP Holes 763B, 765C, 766A, and 1138A (southern Indian Ocean)—reveal varying redox trends. European sections show declining oxygen levels in the upper ocean prior to the $\delta^{13}C$ excursion, and persistent anoxia occurred in Raia del Pedale, a shallow-water platform-carbonate site. Indian Ocean sites record high Ce anomalies (1.0–1.3) in the late Cenomanian followed by low values (~0.4) into the Maastrichtian, indicating persistent deoxygenation. Although much of the upper ocean remained oxic, we utilize thermodynamic modeling to quantify the extent of anoxia in the upper ocean during OAE 2, suggesting significant loss of oxygen therein. This study highlights spatial heterogeneity in ocean deoxygenation during OAE 2 as a combined result of warm climate, ocean circulation and respiration-driven oxygen demand.

1. Introduction

The oxygen content in the modern ocean has been declining substantially (2 %) during the past four decades, and oceanic models project further deoxygenation up to 7 % by the end of the century (Schmidtko et al., 2017). The global ocean has experienced multiple deoxygenation events over Earth's history since global oxidation (Song et al., 2019). The widespread deposition of Cretaceous organic-rich sediments during specific time intervals has been attributed to several so-called oceanic anoxic events (OAEs) during which marine waters were depleted in oxygen at a regional to global scale (Schlanger and Jenkyns, 1976). At the Cenomanian–Turonian boundary (~94 Ma), a large positive carbon-isotope excursion is conventionally used to define the most significant deoxygenation event in the Cretaceous, namely OAE 2 (Arthur et al., 1990; Schlanger et al., 1987; Jenkyns, 2010; Pancost et al., 2004; Trabucho Alexandre et al., 2010; Jenkyns et al., 2017; Owens et al., 2018). This event is hypothesized to have been triggered by massive basalt–seawater interaction (i.e. processes such as volcanism, hydrothermal activity, submarine weathering of mafic igneous rock) related to the formation of one or more Large Igneous Provinces (LIPs) including oceanic plateaus, which caused a cascade of environmental changes ultimately leading to increased global accumulation of organic matter. Evidence for this phenomenon derives from strontium-, osmium- neodymium and mercury isotope profiles (Sinton and Duncan, 1997; Kerr,

☆ This article is part of a special issue entitled: 'In honor of Bill McDonough' published in Geochimica et Cosmochimica Acta.

* Corresponding author at: International Center for Isotope Effects Research, Nanjing University, Nanjing 210023, China.
E-mail address: chengcao@nju.edu.cn (C. Cao).

https://doi.org/10.1016/j.gca.2025.12.022
Received 30 June 2025; Accepted 13 December 2025
Available online 26 December 2025

1998; Jones and Jenkyns, 2001; Turgeon and Brumsack, 2006; Zheng et al., 2013; Du Vivier et al., 2014, 2015; Scaife et al., 2017). A warmer climate (hyperthermal conditions) and long-term sea-level rise accelerated multiple environmental perturbations such as continental and submarine weathering, thereby boosting nutrients for surface-ocean planktonic photosynthesis (e.g. Schlanger et al., 1981; Larson, 1991; Sinton and Duncan, 1997; Bach and Irber, 1998; Kerr, 1998; Adams et al., 2010; Barclay et al., 2010; Blättler et al., 2011; Pogge Von Strandmann et al., 2013; Jenkyns et al., 2017).

Multiple studies have been undertaken to investigate the timing and extent of oceanic anoxia during OAE 2, in both deep water and the upper levels of the ocean (Montoya-Pino et al., 2010; Owens et al., 2013; Zhou et al., 2015; Holmden et al., 2016; Owens et al., 2017; Ostrander et al., 2017; Clarkson et al., 2018; Zhai et al., 2023). Organic-rich black shales that are the hallmark of the event are widely distributed, with a strong bias to the northern hemisphere, particularly in the North Atlantic Ocean, its adjacent epicontinental seas, and the continental margins of the Alpine-Mediterranean Tethys. Sparse occurrences are also documented in the paleo-equatorial Pacific and Indian Oceans (Schlanger et al., 1987; Pancost et al., 2004; Trabucho Alexandre et al., 2010; Owens et al., 2018). In part, this distribution has been hypothesized to be a result of local watermass stratification leading to euxinia, aided by increased fluvial input to the oceans as well as enhanced upwelling in *peri*-equatorial regions (Damsté and Köster, 1998; van Bentum et al., 2009; Jenkyns, 2010). One proposed mechanism for enhanced organic-carbon burial involves increased preservation under anoxic deep-water conditions, which requires that the replenishment of oxygen-rich surface waters occurred more slowly than oxygen consumption during decomposition of organic matter. During the hyperthermal conditions of OAE 2, warming would likely have reduced the oxygen content of surface and deep waters (Blumenberg and Wiese, 2012; Robinson et al., 2019; Damsté et al., 2010). Modelling studies have also suggested sinking saline water derived from tropical shelf seas could have caused the shortage of oxygen supply to the deep ocean, but this hypothesis lacks clear geochemical evidence (Brass et al., 1982; Slingerland et al., 1996; Trabucho Alexandre et al., 2010). Compared to the proto-Atlantic Ocean, the Indian Ocean is less studied, and the drivers to explain different regional deoxygenation and oxygenation patterns during OAE 2 at the global scale have remained less clear.

The extent of anoxia in near-surface waters during OAE 2 varied spatially, as indicated by iodine: calcium ratios (I/Ca) in carbonates (Zhou et al., 2015; Owens et al., 2016a). Additionally, proxy data, including trace-element abundance in carbonate-rich sections, indicate that magnitudes of oxygen depletion in the water column were subject to significant fluctuations during OAE 2 itself with episodes of reoxygenation such as the so-called Plenus Cold Event (Hetzel et al., 2009; Owens et al., 2012; Owens et al., 2013; Goldberg et al., 2016; Jenkyns et al., 2017; Owens et al., 2017; Jenkyns, 2018; O'Connor et al., 2020). Significantly, evidence from Tl isotopes reveals that global deoxygenation predated the OAE or onset of enhanced organic-matter burial as defined by the carbon-isotope excursion (Owens et al., 2017; Ostrander et al., 2017). Another study of the Tarfaya (Morocco) upwelling system in the proto-North Atlantic concluded that the transition of oxic to euxinic conditions happened prior to OAE 2 with a time lag of ~400 kyr, based on nitrogen isotopes, and 115 kyr based on vanadium and molybdenum concentrations (Scholz et al., 2019; Zhai et al., 2023).

To understand the extent that oceanographic changes may have influenced oxygen in the global upper ocean in terms of regional differences, this study compares redox responses between restricted basins and the open ocean using the Ce anomaly in marine carbonates. Rare-earth elements and yttrium (REY) constitute a well-characterized proxy in modern environments and are a promising tool for paleo-redox studies (e.g. Bodin et al., 2013; Tostevin et al., 2016). Under fully oxic conditions, Ce is progressively oxidized from soluble Ce(III) to insoluble Ce(IV), typically accumulating on the surface of ferromanganese oxyhydroxides on the seafloor. Consequently, the residual seawater becomes relatively depleted in Ce compared to other rare-earth elements (German and Elderfield, 1990). The reverse process, namely the reduction of Ce(IV) to Ce(III), which occurs in both anoxic ($O_2 = 0$) and suboxic ($O_2 < 5$ μmol/kg) environments (Rue et al., 1997), increases the cerium content of seawater. The relative enrichment or depletion of Ce relative to its neighbours in the periodic table is usually defined as a Ce anomaly, expressed as $Ce/Ce^* = Ce/(Pr^*(Pr/Nd))$ (Lawrence et al., 2006). Therefore, herewith all concentrations are normalized to UCC (Upper Continental Crust) following the approach of Liu et al. (2019).

The Ce anomaly in bulk marine carbonates should primarily reflect average redox conditions in near-surface waters below the air-sea exchange zone including the depth of the oxycline, which for this study will be considered as upper water column or upper ocean. In any geochemical study of ancient carbonate sediments, a negative Ce anomaly ($Ce/Ce^* < 1$) indicates that the environment was oxic and a positive to absent Ce anomaly ($Ce/Ce^* \geq 1$) indicates a suboxic or anoxic conditions. Importantly, Ce anomalies determined in marine carbonates have been demonstrated to provide a relatively robust Ce/Ce* record of primary seawater values even after recrystallization or dolomitization (Wright et al., 1987; Byrne and Bingler, 1989; Zhong and Mucci, 1995; Webb and Kamber, 2000; Liu et al., 2019; Liu et al. 2021). The relatively short residence time of Ce in seawater (< 500 yr) also makes it a sensitive tracer for redox conditions of sub-basin or watermass over geologically short intervals. OAE 2 is thought to have lasted for 450 to 900 kyr (Voigt et al., 2004; Sageman et al., 2006; Eldrett et al., 2015; Li et al., 2017; Gangl et al., 2019). Additionally, Ce occurs high on the redox ladder compared to other elements such as I (Lu et al., 2010). Thus, Ce can be one of the first elements to record early deoxygenation or re-oxygenation. Herein, well-preserved carbonates from seven Cenomanian–Turonian sections with a global distribution are investigated for Ce anomalies.

2. Materials and methods

2.1. Study sites

Samples derive from three land sections and four Ocean Drilling Program (ODP/IODP) sites (Fig. 1, Table 1). All three outcrop sections are from the northern hemisphere. Eastbourne (southern England), Clot Chevalier (south-east France) and Raia del Pedale (southern Italy) are situated in Europe. The Eastbourne coastal section exposes ~27 m of light-colored pelagic epicontinental Chalk facies, of latest Cenomanian–earliest Turonian age, which was situated in the central part of the Anglo-Paris Basin at an estimated paleodepth of a few hundred meters (Hancock, 1975). Poorly lithified foraminiferal-nannofossil carbonates from this section have very low values of total organic carbon (TOC) and were not subject to appreciable diagenetic sulfate reduction in pore waters (Paul et al., 1999; Keller et al., 2001; Tsikos et al., 2004; Gale et al., 2005), which should have minimized alteration of the primary Ce anomaly. The Clot Chevalier is from the Vocontian Trough, a relatively deep subtropical basin on the northern margin of the Alpine-mediterranean Tethys. The section is ~ 35 m thick and comprises alternating dark gray foraminiferal-nannofossil marlstones and light gray more indurated limestones of latest Cenomanian–earliest Turonian age. Micropalaeontological, lithostratigraphic and sedimentological analyses of nearby sections within the Vocontian Trough indicate deposition in a hemipelagic domain and a paleodepth of a few hundred meters deepening to the north-east (Falzoni et al., 2016b; Gale et al., 2019). Raia del Pedale (Italy), is an organic-lean, platform carbonate dominantly comprising gray calcareous mudstone containing benthic foraminifera and thick-shelled fossils such as rudists. Thin centimeter-scale black laminated carbonates occur at some levels. This 'shallow-water' section was likely deposited in water depths of only a few meters or tens of meters (Parente et al., 2008; Frijia et al., 2019).

The four ODP/IODP holes are situated in the southern Indian Ocean. ODP Sites 763, 765, 766 form a depth transect on the western margin of

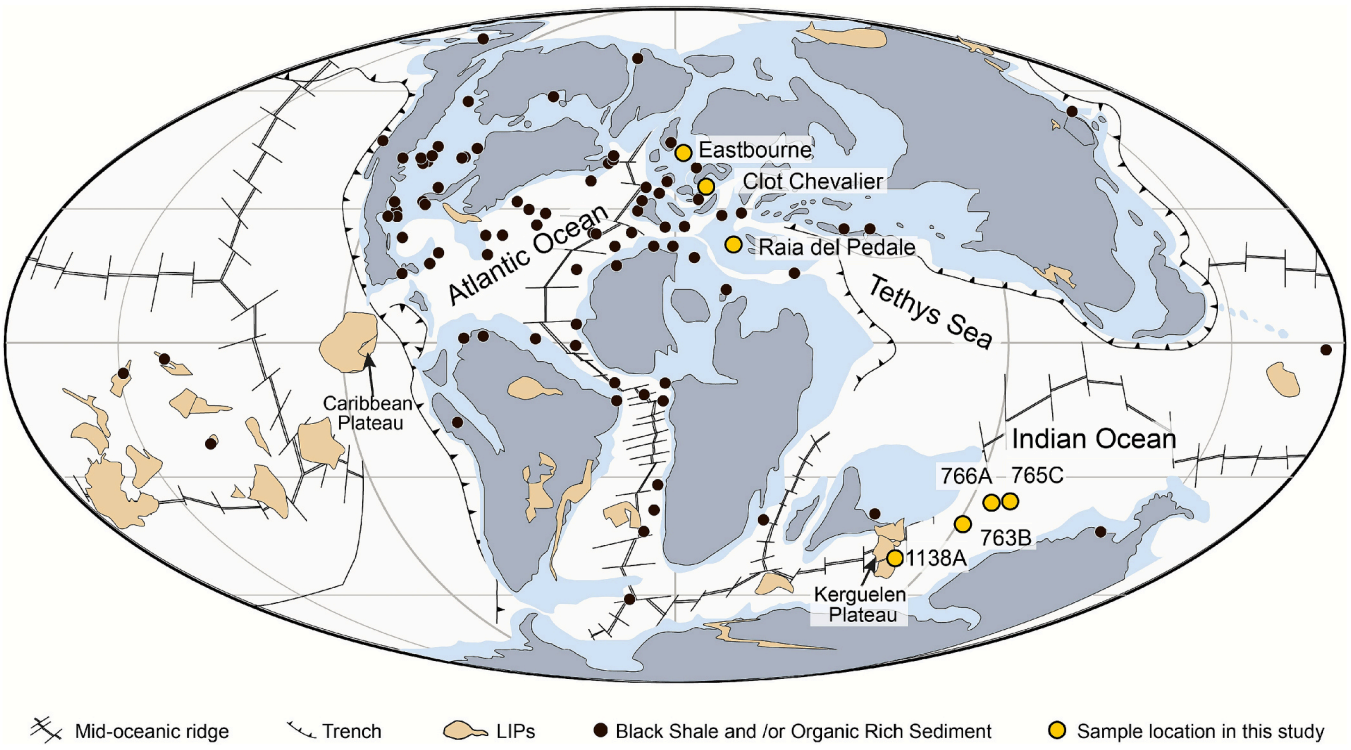

Fig. 1. Sample locations in the mid-Cretaceous (ca. 90 Ma). Black circles represent the location of the OAE-related organic-rich sediments (black shales) and yellow circles show the sampling locations of marine carbonate units. All locations are based on published literature (Arthur et al., 1987; Schlanger et al., 1987; Takashima et al., 2006, 2009; Trabucho Alexandre et al., 2010; Owens et al., 2018;). The distribution of continental masses is based on Scotese (2004) and modified from Trabucho Alexandre et al. (2010). Landmasses and epicontinental seas are marked in gray and light blue. Sample locations for this study are marked in yellow circles (Murphy and Thomas, 2012; Thomas and Tilghman, 2014).

Australia. Hole 763B (Exmouth Plateau; 45°S paleolatitude at 90 Ma) was likely deposited in intermediate depths during the Cretaceous (Haq et al., 1992). Hole 763B recovered upper Albian to lower Campanian nannofossil chalks with clay classified as calcareous claystones to claystones (Haq et al., 1991). ODP Holes 766A and 765C are situated on the Exmouth Plateau and Argo Abyssal Plain, respectively, and they are relatively deep-water sites (Gradstein, 1992). Cenomanian–Maastrichtian sediments from Hole 766A largely comprise zeolitic nannofossil oozes and clays locally pink to pale brown to gray and lighter colored graded foraminiferal-rich levels. Coeval sediments from Hole 765C are broadly similar to those in Hole 766A for the Cenomanian–Turonian interval (Ludden and Gradstein, 1990a). ODP Hole 1138A, which sampled an organic-rich shale of Cenomanian–Turonian boundary age, is located on the Central Kerguelen Plateau and has been suggested to have been deposited in shallow to intermediate water depths as the seafloor underwent thermal subsidence between ~94 Ma and 86 Ma (Dickson et al., 2017; Frey et al., 2000). Sediments at this site are composed of calcareous sandstone and claystone in the Cenomanian and interbedded chalk, nannofossil claystone, and foraminifera-bearing nannofossil chalk in the Turonian–upper Maastrichtian (Dickson et al., 2017).

2.2. Sample preparation and measurements

Samples from the Indian Ocean have no reported mineralogical data. Hence, we semi-quantitively determined the mineralogy of these sample using a Rigaku Miniflex II X-Ray diffractometer at the University of North Carolina at Chapel Hill. We selected samples that contain > 75 % of calcite for sequential leaching. The detailed sample treatment and analytical method used here were previously reported in Cao et al., (2020; 2023). In brief, about 200 mg sample powder were leached using 10 ml of 1 M ammonium acetate, 10 ml of 1 M ammonium carbonate (twice) and 5 ml 0.3 M acetic acid (twice). Only leachates from acetic acid were collected by passing the solution through a 0.22 μm filter and evaporated to dryness in acid-cleaned Teflon beakers. After dissolving in 2 % nitric acid, 1 ml of the leachates was diluted 5-fold for elemental concentration analysis using an Agilent™ 7900 Quadruple ICP-MS (Inductively Coupled Plasma-Mass Spectrometer) at the University of North Carolina at Chapel Hill. Repeated analyses of the certified carbonate material, NIST-SRM-1d, yield analytical reproducibility RSD < 5 % (n = 50) for elemental concentrations. Ultrapure reagents were used for sequential leaching experiments and the procedural blank for trace elements was comparable to the instrumental blank (Cao et al., 2020).

2.3. Modeling oceanic dissolved oxygen using the Ce anomaly

We applied a thermodynamic Ce oxidation model to quantitatively estimate dissolved oxygen loss in the upper water column during OAE 2 at European sites and during long-term warming in the proto-Indian Ocean. This model, based on the oxidation reaction of Ce^{3+} to Ce^{4+} from the dissolved oxygen and the complexation reactions of Ce^{3+} with PO_4^{3-}, CO_3^{2-}, and OH^-, is governed by the general function: $\log(\gamma_i C_{Ce}) = K - \frac{1}{4}\log(pO_2) + \partial_i \log\{\mathscr{X}_i\} - \beta_i pH$(Cao et al., 2022). Here, the C_{Ce} is the total dissolved Ce, and γ_i represents the relative activity coefficient for trivalent Ce species including $CePO_4^0$, $CeCO_3^+$, and $Ce(CO_3)_2^-$ (Cantrell and Byrne, 1987; Nakada et al., 2017; Byrne et al., 1991). The terms $(\partial_i, \mathscr{X}_i)$ and βi correspond to the complexing ligands and pH sensitivity, and are expressed as $(1, PO_4^{3-})$, $(1, HCO_3^-)$, or $(2, CO_3^{2-})$, β_i ranges from 1 to 3, depending on each complexation reaction. The model is particularly effective for reconstructing paleo-redox conditions during transitions from oxic to suboxic-anoxic states, as the Ce anomaly is highly sensitive to dissolved oxygen in suboxic to anoxic waters ($pO_2 < 0.01$ atm) but loses sensitivity in fully oxygenated environments (Cao et al., 2022). Validation with modern ocean profiles indicates that the phosphate

Table 1
Ce anomaly and preservation quality assessment based on elemental ratios in the leachate fraction.

	No.	Sample ID	Depth (mbsf)	Age (Ma)	Ce/Ce*	εNd(t)	Mg/Ca mol/mol	Al/Ca mmol/mol	Mn/Ca mmol/mol	Sr/Ca mmol/mol	Fe/Ca mmol/mol	Rb/Sr mmol/mol	Mn/Sr mol/mol	Y/Ho g/g	Total REE/Ca g/g	La/La*	Eu/Eu*	Yb/Nd	Nd/Nd*
763B	1	13–5, 52–54	296.01	79.33	0.49		0.00	0.05	0.22	0.88	0.01	0.12	0.25	37.45	0.05	2.83	1.39	2.58	1.20
	2	14–1, 131–133	305.32	80.80	0.40	−8.20	0.00	0.04	0.33	0.89	0.01	0.11	0.37	39.39	0.06	2.85	1.45	2.59	1.16
	3	14–5, 82–84	310.83	81.67	0.42		0.00	0.04	0.57	0.89	0.04	0.12	0.64	37.80	0.05	3.02	1.77	2.71	1.17
	4	15–1, 116–118	314.67	82.28	0.49	−7.80	0.00	0.03	0.24	0.83	0.00	0.25	0.29	38.22	0.03	3.24	1.70	2.76	1.21
	5	15–5, 50–52	319.40	83.03	0.41		0.00	0.03	0.14	0.79	0.01	0.09	0.18	38.50	0.04	3.01	2.66	3.00	1.11
	6	16–1, 91–93	323.92	83.75	0.50	−7.70	0.00	0.01	0.12	0.81	0.00	0.20	0.15	49.13	0.01	5.54	10.97	2.93	1.29
	7	17–1, 117–119	333.68	85.30	0.52	−7.70	0.00	0.02	0.24	0.77	0.00	0.36	0.30	39.01	0.03	3.20	1.69	2.91	1.20
	8	17–4, 75–77	337.76	85.92	0.37		0.00	0.03	0.25	0.65	0.00	0.30	0.38	36.06	0.05	2.49	1.50	2.46	1.17
	9	18–1, 42–44	342.43	86.63	0.45	−7.80	0.00	0.09	0.30	0.62	0.01	0.43	0.49	32.04	0.11	1.63	1.87	2.14	1.01
	10	18–3, 53–55	340.54	86.35	0.51		0.00	0.03	0.44	0.63	0.00	0.30	0.69	38.29	0.05	2.47	2.83	3.26	1.09
	11	19–1, 87–89	352.38	88.13	comtamination	−8.40	0.00	18.02	0.40	3.22	1.86	9.02	0.12	36.84	108.67	2.09	2.42	2.19	1.06
	12	19–5, 45–47	357.96	88.96	0.46		0.00	0.06	0.52	0.50	0.01	0.59	1.04	32.55	0.09	1.77	2.04	2.48	1.04
	13	20–1, 26–28	361.27	89.45	0.45		0.00	0.10	0.55	0.54	0.01	0.38	1.00	30.52	0.10	1.65	1.92	2.68	1.03
	14	21-CC, 16–18	373.25	91.23			0.00	6.93	0.20	8.74	1.99	6.47	0.02	21.73	0.08	1.03	160.67	3.21	0.93
	15	22–1, 17–19	380.18	92.26	0.60		0.00	0.39	0.82	0.94	0.05	0.22	0.87	33.03	0.13	1.57	1.98	1.59	1.01
	16	22-CC, 25–27	381.95	92.52	0.75		0.00	0.53	1.89	0.65	0.11	0.24	2.90	32.96	0.16	1.53	1.64	2.34	0.97
	17	23–1, 134–136	390.85	93.84	0.90		0.00	0.52	2.04	1.21	0.14	0.16	1.69	32.53	0.13	1.45	1.98	1.77	0.91
	18	23–3, 16–18	392.67	94.11	0.89	−10.50	0.00	0.70	1.92	1.42	0.18	0.25	1.35	32.37	0.16	1.33	1.80	1.33	0.98
	19	23–5, 45–47	391.06	93.89	0.84		0.00	0.31	3.18	1.15	0.08	0.10	2.77	32.48	0.11	1.41	2.15	1.88	0.95
	20	24–1, 115–117	400.16	95.13	diagenesis	−11.10	0.00	0.33	3.89	1.25	0.04	0.15	3.11	33.97	0.12	1.51	2.21	2.14	0.95
	21	24–3, 81–83	402.82	95.83	0.93	−10.70	0.00	0.63	2.29	1.40	0.14	0.17	1.64	32.83	0.13	1.51	2.10	1.87	0.97
	22	24–5, 37–39	405.38	96.18	0.90		0.00	0.87	1.32	1.51	0.19	0.17	0.88	31.05	0.15	1.38	2.00	1.32	0.95
	23	19–3, 61–62	355.10	89.28	0.52		0.00	0.03	0.71	0.63	0.00	0.29	1.13	38.18	0.05	2.71	2.83	2.51	1.14
	24	19–6, 61–63	359.62	89.99	0.52	−8.00	0.00	0.03	0.72	0.54	0.01	0.40	1.34	36.06	0.08	2.15	2.26	2.20	1.04
	25	20–1, 33.5–34.5	361.34	90.26	0.40	−7.50	0.00	0.06	0.55	0.60	0.02	0.42	0.92	32.00	0.11	1.69	2.01	1.79	1.05
	26	20–2, 95–96	363.45	90.59	0.38	−7.50	0.00	0.03	0.65	0.61	0.01	0.28	1.08	37.31	0.07	2.43	2.23	1.79	1.13
	27	21–1, 8–9	370.59	91.70	0.79	−9.40	0.00	0.04	0.87	0.59	0.00	0.21	1.48	36.34	0.06	2.21	3.07	2.33	1.06
	28	21–1, 118.5–119.5	371.69	91.88	0.42	−8.70	0.00	0.13	1.48	0.64	2.00	0.13	2.32	34.60	0.07	1.73	1.78	2.63	1.04
	29	21–2, 69–70	372.70	92.03	0.81	−9.50	0.00	0.04	1.03	0.53	0.00	0.22	1.96	38.09	0.07	2.05	2.63	2.49	1.04
	30	22–1, 85.5–86.5	380.86	93.31	0.68	−10.90	0.00	0.06	1.68	0.83	0.01	0.22	2.04	33.34	0.14	1.68	2.13	1.85	1.01
	31	22–2, 18–19	381.69	93.44	0.74	−10.70	0.00	0.10	1.79	0.75	0.02	0.17	2.40	34.49	0.13	1.77	2.15	2.11	1.03
	32	23–1, 43–44	389.94	94.54	diagenesis	−10.50	0.00	0.08	4.11	0.96	0.01	0.16	4.29	36.12	0.09	1.55	2.62	2.16	0.94
	33	23–2, 33–34	391.34	94.72	0.94	−10.40	0.00	0.32	2.73	1.29	0.08	0.24	2.12	34.11	0.15	1.48	2.03	1.53	1.00
	34	23–4, 55–56	394.56	95.13	0.78	−10.80	0.00	0.26	3.04	1.36	0.07	0.15	2.24	34.33	0.12	1.38	2.07	1.44	0.94
	35	23–5, 41.5–42.5	395.92	95.31	0.87	−10.40	0.00	0.38	3.18	1.32	0.13	0.17	2.41	34.42	0.14	1.37	2.16	1.42	0.98
	36	24–7, 30.5–31.5	408.31	96.90	0.98	−10.30	0.00	0.57	2.54	1.62	0.18	0.23	1.56	35.28	0.18	1.43	2.00	1.27	0.97
	37	25–1, 45–46	408.455	96.98	1.27	−10.10	0.00	0.60	4.29	1.60	0.06	0.32	2.68	36.60	0.35	1.96	1.81	0.96	1.13
	38	25–3, 50.5–51.5	412.01	97.37	1.17	−10.10	0.00	1.45	1.17	1.75	0.21	0.28	0.67	33.78	0.26	1.22	1.80	0.94	0.97
	39	26–3, 81–82	421.81	98.63	1.08	−9.70	0.00	1.88	4.37	1.46	0.13	0.42	2.98	32.92	0.44	1.22	1.56	1.00	0.98
	40	27–4, 85–86	432.85	100.04	diagenesis	−9.30	0.00	0.86	8.51	1.10	0.49	0.24	7.77	35.29	0.17	1.55	1.90	1.79	1.03
	41	28–4, 82–84	442.35	101.26	diagenesis	−9.70	0.00	0.74	8.42	1.12	0.49	0.25	7.53	36.10	0.19	1.54	1.83	1.91	0.93
765C	1	23–2, 35–37	561.55	75.02	comtamination	−10.4	0.00	24.95	1.98	0.70	1.33	10.82	2.85	25.30	0.30	0.72	0.95	1.43	0.72
	2	23–4, 22–24	564.43	76.61	1.17	−8.4	0.00	0.52	2.26	1.06	0.02	0.12	2.13	32.09	0.12	1.56	1.75	2.54	0.97
	3	24–4, 6–8	573.82	84	0.38		0.00	0.19	1.52	0.73	0.01	0.14	2.09	28.31	0.17	1.54	1.38	2.83	0.99
	4	25–1, 37–39	579.3	87.40	0.37		0.00	0.27	1.16	0.57	0.01	0.33	2.05	29.54	0.17	1.51	1.41	2.22	0.99
	5	25–1, 99.0–101.0	580	87.83	0.35		0.00	0.09	1.10	0.57	0.13	0.21	1.92	29.86	0.14	1.57	1.49	2.76	0.98
	6	25–3, 4–6	582	89.07	0.60		0.00	0.44	1.25	0.70	0.01	0.19	1.78	29.09	0.15	1.66	1.91	2.99	0.95
	7	25–4, 53–55	584.5	90.62	0.62	−7.7	0.00	0.43	1.44	0.64	0.02	0.19	2.24	30.98	0.17	1.69	1.70	2.75	1.00
	8	25–5, 33–35	585.37	91.51	0.60	−7.3	0.00	0.41	1.48	0.63	0.01	0.24	2.37	29.76	0.21	1.55	1.64	2.30	1.00

(*continued on next page*)

Table 1 (*continued*)

	No.	Sample ID	Depth (mbsf)	Age (Ma)	Ce/Ce*	εNd(t)	Mg/Ca mol/mol	Al/Ca mmol/mol	Mn/Ca mmol/mol	Sr/Ca mmol/mol	Fe/Ca mmol/mol	Rb/Sr mmol/mol	Mn/Sr mol/mol	Y/Ho g/g	Total REE/Ca g/g	La/La*	Eu/Eu*	Yb/Nd	Nd/Nd*
	9	26–2, 94–96	590.9	96.29	0.75	−8.4	0.00	0.74	1.83	0.71	0.01	0.21	2.58	30.96	0.15	1.85	1.97	3.54	0.94
	10	26–3, 79–81	592.02	98.17	comtamination	−8.2	0.00	67.69	15.11	1.53	0.91	6.84	9.88	23.09	2.74	0.86	1.28	0.89	0.82
	11	26–5, 41–43	594.17	101.24	comtamination	−8.2	0.00	15.07	2.77	0.80	0.28	2.23	3.45	23.25	4.05	0.83	1.17	0.86	0.88
	12	25–3, 61–62	582.6	90.01	comtamination	−6.7	0.00	8.71	1.93	0.82	0.86	1.37	2.35	25.20	1.35	0.96	1.33	0.89	0.89
	13	25–5,49.5–50.5	585.53	91.96	0.74	−7.2	0.00	0.23	2.72	0.51	0.00	0.42	5.35	30.76	0.18	1.85	1.73	2.14	1.02
	14	26–1, 4–5	588.34	93.83	0.71	−7.1	0.00	2.97	1.20	0.64	0.03	0.92	1.88	28.50	1.00	1.15	1.36	1.05	0.96
	15	26–1, 34–35	588.64	94.03	0.45	−6.7	0.00	1.47	1.57	0.70	0.01	0.49	2.23	28.04	0.42	1.44	1.54	1.62	0.93
	16	26–1, 57–58	588.87	94.19	comtamination	−6.3	0.00	126.40	29.10	4.79	0.98	4.22	6.08	24.41	12.09	1.12	1.31	1.02	0.89
	17	26–1, 84–85	589.13	94.73	0.68	−7.4	0.00	1.33	1.78	0.69	0.01	0.44	2.59	28.66	0.42	1.37	1.57	1.53	0.94
	18	26–2, 24–25	589.98	95.95	0.63	−7.7	0.00	0.59	1.75	0.73	0.01	0.24	2.42	28.58	0.17	1.77	1.66	3.26	0.93
	19	26–2, 55.5–56.5	590.3	96.4	0.85	−7.7	0.00	0.72	1.75	0.70	0.02	0.27	2.49	29.51	0.18	1.72	1.85	3.07	0.92
	20	26–2, 64–65	590.4	96.55	0.83	−7.7	0.00	0.59	1.84	0.71	0.01	0.23	2.60	30.93	0.18	1.70	1.77	3.04	0.92
	22	26–4, 28–29	592.93	100.16		−8.4	0.00	142.14	3.33	3.05	1.72	6.96	1.09	22.53	13.49	0.83	1.25	0.70	0.84
	23	26–2, 7.5–8.5	589.83	95.73		−6.7	0.00	200.36	28.46	4.38	1.63	3.41	6.50	23.60	18.18	0.89	1.58	0.68	0.88
	24	26–1, 136–137	589.65	95.48	0.55	−6.6	0.00	0.54	1.65	0.76	0.01	0.29	2.16	27.80	0.20	1.67	1.77	2.68	0.98
766A	1	11–1, 107–109	95.48	71.62	0.44		0.00	0.05	0.06	1.00	0.00	0.14	0.06	29.02	0.07	1.82	1.16	1.61	1.03
	2	11–2, 117–119	97.38	72.40	0.39	−9.85	0.00	0.03	0.05	1.16	0.00	0.11	0.04	33.69	0.02	2.96	1.41	1.47	1.15
	3	11–3, 60–62	98.31	72.78	0.61	−9.73	0.00	0.04	0.07	1.13	0.00	0.12	0.06	34.83	0.04	3.00	1.73	2.05	1.09
	4	11–4, 79–81	100	73.46	0.39	−10.13	0.00	0.04	0.05	1.19	0.00	0.12	0.04	31.70	0.05	2.14	1.32	1.40	1.08
	5	11–5, 33–35	101.04	73.88	0.45	−9.89	0.00	0.02	0.05	1.12	0.00	0.10	0.04	34.16	0.03	2.72	1.46	1.68	1.06
	6	12–1, 119–121	105.5	75.67	0.43	−9.89	0.00	0.04	0.04	1.11	0.00	0.14	0.04	33.13	0.03	2.75	1.33	1.72	1.08
	7	12–2, 10–12	105.91	75.84	0.37	−9.89	0.00	0.03	0.04	1.06	0.00	0.11	0.04	32.57	0.04	2.55	1.28	1.40	1.08
	8	13–1, 87–89	114.78	82.68	0.30	−7.29	0.00	0.24	0.08	0.92	0.01	0.33	0.09	27.51	0.09	2.01	2.11	1.81	1.01
	9	13–2, 98–100	115.92	83.00	0.28		0.00	0.11	0.11	0.83	0.00	0.26	0.14	26.23	0.08	1.81	1.94	1.50	1.00
	10	13–3, 97–99	117.88	85.16	0.30	−5.99	0.00	0.11	0.10	0.61	0.00	0.52	0.17	29.25	0.06	2.22	2.52	1.16	1.10
	11	14–4, 35–37	128.46	90.14	0.33	−6.71	0.00	0.08	0.10	0.40	0.00	0.60	0.24	30.12	0.07	2.11	2.62	1.53	1.02
	12	14–2, 87–89	125.98	88.59	0.27	−5.47	0.00	0.31	0.10	0.38	0.01	0.99	0.27	28.62	0.16	1.77	2.01	1.47	1.00
	13	14–3, 56–58	127.17	89.42	0.13	−5.63	0.00	0.11	0.06	0.56	0.01	0.39	0.10	23.81	0.15	1.39	1.59	1.77	0.93
	14	14–4, 66–68	128.77	90.31	0.34	−5.87	0.00	0.11	0.07	0.50	0.00	0.53	0.14	28.62	0.08	2.03	2.49	2.56	0.97
	15	14–5, 45–47	130.06	91.02	0.28	−7.28	0.00	0.10	0.05	0.57	0.01	0.21	0.09	28.81	0.15	1.59	1.55	1.89	0.99
	16	15–1, 38–40	133.58	93.06	0.34		0.00	0.25	0.13	0.63	0.01	0.40	0.20	26.94	0.19	1.54	1.68	1.96	0.90
	17	15–2, 17–19	134.88	93.81	0.26	−6.21	0.00	0.12	0.08	0.73	0.01	0.26	0.10	26.52	0.15	1.56	1.44	2.11	0.90
	18	15–4, 104–106	138.75	96.8	0.87	−8.48	0.00	0.21	0.46	0.62	0.00	0.30	0.75	29.01	0.15	1.67	1.38	2.09	0.95
	19	15–5, 34–36	139.55	97.41	0.93	−8.28	0.00	0.15	0.62	0.73	0.01	0.26	0.86	27.94	0.14	1.69	1.57	2.42	0.93
	20	15–6, 25–27	140.96	97.93	0.67	−8.43	0.00	0.32	0.52	0.69	0.02	0.42	0.76	26.19	0.26	1.47	1.42	1.50	0.92
	21	16–1, 47–49	143.38	98.61	0.81	−8.24	0.00	0.27	0.51	0.57	0.00	0.58	0.90	28.39	0.15	1.62	1.58	1.67	0.93
	22	16–2, 97–99	145.38	99.17	0.56	−8.72	0.00	0.09	0.14	0.72	0.00	0.26	0.19	28.69	0.07	2.18	1.66	1.78	1.01
	23	16–3, 113–115	147.04	99.64	0.78	−7.83	0.00	0.07	0.17	0.82	0.01	0.22	0.21	30.14	0.06	2.40	1.59	2.29	1.04
	24	16–4, 29–31	147.7	99.82	0.78	−8.09	0.00	0.09	0.20	0.79	0.00	0.29	0.26	29.16	0.08	2.15	1.63	1.98	1.02
	25	16–5, 86–88	149.77	101.7	0.58	−8.8	0.00	0.11	0.13	0.72	0.00	0.36	0.19	26.27	0.09	1.58	1.46	1.92	0.90
	26	16–6, 22–24	150.63	100.7	0.53	−8.17	0.00	0.05	0.13	0.65	0.00	0.45	0.19	28.18	0.08	1.84	1.64	1.53	0.97
	27	11–6, 40–42	102.61	74.51	0.35	−9.81	0.00	0.02	0.04	1.12	0.00	0.11	0.04	35.17	0.04	2.40	1.25	1.37	1.04
	28	11–7, 21–23	103.92	75.04	0.39	−9.87	0.00	0.03	0.05	0.98	0.00	0.18	0.05	33.60	0.03	2.69	1.29	1.31	1.09
	29	14–4, 146.5–147.5	129.56	91.42	0.30	−7.3	0.00	0.04	0.07	0.62	0.00	0.26	0.11	32.21	0.06	2.42	2.42	2.05	1.05
	30	14–5, 70.5–71.5	130.3	91.76	0.39	−6.8	0.00	0.05	0.05	0.53	0.00	0.46	0.09	30.60	0.07	2.16	2.39	2.17	1.03
	31	15–1, 8–9	133.26	93.11	0.30	−5.3	0.00	0.07	0.07	0.47	0.00	0.39	0.14	28.98	0.09	1.85	1.73	2.14	0.96
	32	15–1, 115–116	134.35	93.55	0.31	−6.6	0.00	0.27	0.09	0.63	0.01	0.52	0.14	27.81	0.19	1.50	1.60	1.39	0.97
	33	15–2, 55–56	135.26	94.63	comtamination	−6.4	0.00	196.29	11.13	3.89	1.01	5.45	2.86	22.89	8.20	0.87	1.50	0.76	0.78
	34	15–2, 94–95	135.64	95.09	comtamination	−7.9	0.00	200.54	26.62	3.02	3.45	15.14	8.80	22.27	4.30	0.97	2.53	0.64	0.84
	35	15–3, 12–13	136.32	95.89	0.95	−8.5	0.00	0.07	0.84	0.62	0.01	0.31	1.35	29.77	0.10	2.26	1.74	2.02	1.04
	36	15–3 29–30	136.49	96.10	comtamination	−6.5	0.00	2.59	0.16	0.70	0.04	1.71	0.22	27.17	1.54	1.15	1.32	0.69	0.99

(*continued on next page*)

Table 1 (*continued*)

	No.	Sample ID	Depth (mbsf)	Age (Ma)	Ce/Ce*	εNd(t)	Mg/Ca mol/mol	Al/Ca mmol/mol	Mn/Ca mmol/mol	Sr/Ca mmol/mol	Fe/Ca mmol/mol	Rb/Sr mmol/mol	Mn/Sr mol/mol	Y/Ho g/g	Total REE/Ca g/g	La/La*	Eu/Eu*	Yb/Nd	Nd/Nd*
	37	15–3, 38.5–39.5	136.58	96.20	1.00	−7.5	0.00	0.05	0.91	0.63	0.00	0.26	1.46	30.08	0.08	2.21	1.87	2.19	1.00
	38	15–3, 46.5–47.5	136.68	96.32	0.75	−7.6	0.00	0.05	0.30	0.70	0.01	0.23	0.42	27.64	0.12	2.02	1.81	1.82	0.97
	39	15–3, 99–100	137.2	96.94	1.02	−8.1	0.00	0.13	0.97	0.57	0.01	0.39	1.70	28.08	0.17	1.80	1.58	1.77	0.95
	40	15–4, 69–70	138.38	98.35	0.70	−8.3	0.00	0.06	0.36	0.72	0.01	0.20	0.50	31.15	0.09	2.11	1.47	1.96	1.04
	41	15–5, 100–101	140.2	100.1	0.76	−8.5	0.00	0.11	0.51	0.76	0.00	0.25	0.68	28.19	0.12	1.87	1.61	2.26	0.97
1138A	1	67–2, 5–6	632.17	86.4	0.62	−6.7	0.00	0.08	0.58	0.97	0.79	0.26	0.59	29.00	0.08	1.51	1.86	1.62	1.00
	2	67–2, 75–76	632.87	92.99	0.63	−5.4	0.00	0.15	1.02	0.81	2.32	0.19	1.26	30.12	0.08	1.62	1.62	2.77	0.92
	3	68–1, 6–7	640.47	93.31	0.58	−6.8	0.00	0.03	1.23	1.11	1.22	0.16	1.11	32.34	0.07	1.56	1.62	2.13	0.97
	4	68–1, 42.5–43.5	640.835	93.33	0.56	−6.6	0.00	0.17	1.28	0.89	1.75	0.14	1.44	33.63	0.07	1.54	1.52	1.92	0.98
	5	68–2, 36–37	642.12	93.44	0.67	−7.2	0.00	0.13	1.10	0.81	1.45	0.24	1.36	29.82	0.09	1.34	1.84	1.63	0.97
	6	68–3, 21–22	643.45	93.5	0.68	−1.8	0.00	0.08	1.40	0.91	1.10	0.24	1.55	29.83	0.09	1.42	1.67	1.38	0.91
	7	68–4, 25.5–26.5	644.92	93.53	0.58	−7.5	0.00	0.16	0.96	0.84	0.90	0.20	1.15	29.09	0.08	1.28	1.94	1.51	0.98
	8	69–2, 52.5–53.5	651.95	93.71	0.62	−8	0.00	0.16	1.49	1.05	1.16	0.17	1.42	31.57	0.12	1.38	1.60	1.67	0.97
	9	69–5, 60–61	656.18	93.83	0.62	−8.4	0.00	3.53	0.33	7.69	6.44	0.63	0.04	33.68	1.13	1.16	1.26	0.78	1.01
	10	69–6, 52–53	657.6	93.87	1.09	−5.1	0.00	0.73	0.31	1.78	0.55	0.91	0.18	24.81	0.10	1.18	1.40	0.80	0.88
	11	70–1, 17.5–18.5	659.78	93.94	diagenesis	−2.6	0.00	0.28	2.51	0.31	1.96	0.35	8.21	21.08	0.14	1.09	1.31	0.78	0.91
	12	70–1, 130–131	660.95	93.97	diagenesis	−2.6	0.00	0.25	1.83	0.34	1.02	0.52	5.41	20.66	0.20	1.02	1.31	0.96	0.88
	13	70–2, 56–57	661.67	93.99	diagenesis	−2.3	0.00	0.11	1.77	0.30	0.93	0.48	5.82	20.68	0.19	1.04	1.34	0.96	0.90
	14	71–2, 60–62	671.1	94.27	0.99	−1.3	0.00	1.04	0.86	1.42	0.46	0.95	0.60	19.69	0.22	1.00	1.38	1.10	0.83
	15	72–2, 20–21	680.6	94.54	1.23	0.9	0.00	4.30	11.24	2.54	3.93	0.53	4.42	27.06	0.04	1.43	1.50	1.03	1.15
	16	54–2, 20–22	507.32	68.61	0.46		0.00	0.03	0.51	1.07	0.36	0.08	0.48	35.49	0.05	2.05	2.07	2.49	1.05
	17	56–2, 52–54	526.9	71.94	0.27		0.00	0.02	0.20	1.14	0.44	0.08	0.18	46.51	0.03	4.06	4.11	2.14	1.21
	18	57–1, 61–63	535.1	73.34	0.36	−8.7	0.00	0.02	0.45	0.99	0.43	0.07	0.46	41.73	0.02	3.73	6.12	3.08	1.14
	19	59–1, 50–52	554.11	76.39	0.27	−8.4	0.00	0.01	0.18	0.91	0.46	0.08	0.20	44.74	0.03	3.57	3.51	2.53	1.17
	20	60–2, 22–24	565.04	77.55	0.25	−8.2	0.00	0.01	0.19	0.81	0.55	0.05	0.23	45.56	0.03	3.74	3.53	2.48	1.23
	21	61–1, 48–50	573.4	78.44	0.25	−8	0.00	0.02	0.18	0.83	0.71	0.06	0.21	41.99	0.06	2.60	2.67	1.11	
	22	62–1, 30–32	582.81	79.44	0.25		0.00	0.02	0.14	0.92	0.50	0.10	0.15	44.13	0.04	3.42	3.00	2.52	1.19
	23	63–1, 40–42	592.61	80.48	0.27	−8	0.00	0.02	0.15	0.70	0.51	0.12	0.22	41.94	0.04	3.01	2.68	2.11	1.20
	24	64–1, 72–74	602.53	81.54	0.29	−7.9	0.00	0.01	0.21	0.72	0.71	0.07	0.30	42.84	0.04	3.01	2.90	2.75	1.18
	25	65–1, 58–60	612.09	82.56	0.29	−8.2	0.00	0.03	0.29	0.61	0.86	0.10	0.47	42.24	0.04	2.75	2.26	2.36	1.12
	26	66–1, 49–51	621.6	84.15	0.41	−7.8	0.00	0.02	0.35	0.85	1.34	0.08	0.41	39.58	0.05	2.12	2.13	2.87	1.05
	27	67–1, 95–97	631.66	85.85	0.40	−7	0.00	0.13	1.43	0.62	1.90	0.27	2.31	36.47	0.08	1.66	1.71	2.27	0.97
	28	69–1, 57–59	650.58	93.48	0.62	−4.4	0.00	0.41	1.25	1.21	1.02	0.14	1.03	31.01	0.15	1.37	1.59	1.40	0.98
	29	69–3, 23.5–24.5	652.83	93.73	0.64	−7.5	0.00	0.72	0.84	0.82	0.78	0.49	1.02	32.84	0.18	1.25	1.63	0.73	0.98
	30	73–2, 46–47	689.75	94.81	diagenesis		0.00	12.20	110.39	3.48	20.49	2.12	31.68	22.91	0.14	0.64	1.65	0.81	0.79
CDC			cm																
	1		30		0.84		0.00	0.00	0.31	1.94	2.20	0.27	0.16	33.52	0.29	0.44	1.10	1.25	0.90
	2		293		1.13		0.00	0.00	0.02	0.18	0.08	0.08	0.14	34.89	0.01	0.40	1.23	1.11	0.87
	3		300		0.89		0.00	0.00	0.44	1.58	1.85	0.30	0.28	34.91	0.49	0.40	1.29	1.16	0.95
	4		600		0.72		0.00	0.00	0.54	1.78	2.56	0.26	0.30	35.42	0.72	0.39	1.21	1.16	0.91
	5		930		0.79		0.00	0.00	0.38	1.72	2.65	0.29	0.22	35.87	0.96	0.38	1.17	0.97	0.96
	6		1290		0.75		0.00	0.00	0.36	1.53	2.43	0.34	0.23	38.29	0.66	0.34	1.15	1.04	0.97
	7		1440		0.66		0.00	0.00	0.31	1.44	2.76	0.34	0.22	36.70	0.81	0.28	1.13	1.17	0.95
	8		1770		0.76		0.00	0.00	0.26	1.54	2.80	0.41	0.17	38.84	1.02	0.30	1.14	1.19	0.96
	9		1950		0.61		0.00	0.00	0.32	1.81	5.07	0.13	0.18	41.86	0.45	0.21	1.09	1.21	0.94
	10		2520		0.68		0.00	0.00	0.26	1.44	1.58	0.28	0.18	38.28	0.58	0.28	1.19	1.25	0.97
	11		2730		0.64		0.00	0.00	0.32	1.35	1.81	0.38	0.24	36.77	0.58	0.32	1.19	1.18	0.97
	12		3390		0.56		0.00	0.00	0.33	1.54	2.04	0.11	0.21	40.84	0.30	0.22	1.22	1.39	1.04
			m																
RDP	1		3		1.06		0.00	0.00	0.02	0.18	0.09	0.05	0.13	31.99	0.018	1.26	1.14	0.75	0.90
	2		20		1.46		0.00	0.04	0.01	0.24	0.03	0.04	0.05	37.70	0.008	1.81	1.48	1.01	1.33
	3		34		1.28		0.00	0.03	0.01	0.18	0.04	0.06	0.08	35.45	0.013	1.85	1.07	1.71	0.96

(*continued on next page*)

Table 1 (*continued*)

	No.	Sample ID	Depth (mbsf)	Age (Ma)	Ce/Ce*	εNd(t)	Mg/Ca mol/mol	Al/Ca mmol/mol	Mn/Ca mmol/mol	Sr/Ca mmol/mol	Fe/Ca mmol/mol	Rb/Sr mmol/mol	Mn/Sr mol/mol	Y/Ho g/g	Total REE/Ca g/g	La/La*	Eu/Eu*	Yb/Nd	Nd/Nd*
	4		47		1.41		0.00	0.04	0.01	0.31	0.02	0.05	0.04	41.07	0.005	1.78	1.35	2.99	0.86
	5		77		1.17		0.00	0.02	0.03	0.18	0.02	0.08	0.15	34.80	0.005	1.96	1.55	0.78	0.81
	6		82.25		1.11		0.00	0.05	0.02	0.18	0.07	0.06	0.13	37.42	0.025	1.18	1.19	1.15	0.93
	7		137		1.74		0.00	0.03	0.01	0.27	0.02	0.07	0.04	40.69	0.003	3.47	2.41	0.84	1.91
	8		149		1.09		0.00	0.06	0.01	0.31	0.03	0.11	0.02	44.24	0.02	1.00	1.20	1.17	0.88
	9		177		0.98		0.00	0.04	0.01	0.33	0.04	0.11	0.02	47.04	0.005	2.35	2.04	1.14	1.12
	10		190		1.41		0.00	0.01	0.01	0.31	0.02	0.04	0.02	60.33	0.001	2.43	13.55	2.08	3.84
	11		217		1.09		0.00	0.09	0.01	0.39	0.04	0.10	0.02	38.22	0.02	0.90	1.24	0.90	0.97
	12		242		1.38		0.00	0.02	0.01	0.18	0.06	0.03	0.05	45.93	0.002	1.87	2.71	2.48	0.82
	13		260		1.11		0.00	0.02	0.05	0.15	0.03	0.00	0.31	48.58	0.004	2.00	1.98	2.54	0.87
	14		280		0.80		0.00	0.07	0.04	0.12	0.16	0.34	0.31	40.32	0.02	2.10	1.18	1.93	1.17
	15		293		0.59		0.00	0.27	0.32	1.76	5.05	0.11	0.18	42.01	0.44	1.47	1.13	1.22	0.94
	16		316 cm		1.06		0.00	0.15	0.02	0.19	0.24	0.16	0.09	32.01	0.02	1.04	1.10	0.88	0.88
Eastbourne	1	WC++600	1840		0.55		0.00	0.00	0.63	0.53	0.72	0.16	1.19	39.69	0.23	1.60	1.13	1.25	1.04
	2	WC++350	1590		0.59		0.00	0.00	0.94	0.65	0.92	0.43	1.45	36.81	0.45	1.48	1.12	1.16	0.99
	3	WC++250	1490		0.56		0.00	0.00	0.97	0.51	1.19	0.37	1.90	37.83	0.35	1.54	1.12	1.18	0.99
	4	WC++200	1440		0.53		0.00	0.00	0.84	0.49	1.18	0.32	1.72	38.14	0.38	1.55	1.06	1.24	1.01
	5	PM++100	1340		0.57		0.00	0.00	0.95	0.61	1.50	0.30	1.55	34.96	0.38	1.73	1.15	1.67	1.03
	6	PM++60	1330		0.55		0.00	0.00	1.39	0.58	1.48	0.26	2.41	36.12	0.44	1.56	1.22	1.27	0.98
	7	PM++20	1260		0.59		0.00	0.00	1.15	0.70	1.85	0.28	1.64	36.03	0.55	1.47	1.14	1.21	0.96
	8	PM + 600	1200		0.67		0.00	0.00	0.94	0.83	1.54	0.23	1.12	33.71	0.65	1.39	1.10	1.30	0.97
	9	PM + 540	1140		0.65		0.00	0.00	0.92	0.96	0.92	0.30	0.95	35.12	0.59	1.45	1.09	1.07	1.01
	10	PM + 480	1080		0.60		0.00	0.00	1.04	0.78	1.34	0.29	1.33	35.17	0.44	1.42	1.04	1.26	0.97
	11	PM + 400	1000		0.66		0.00	0.00	0.87	0.88	1.09	0.34	0.99	34.27	0.51	1.39	1.08	1.12	0.97
	12	PM + 200	800		0.79		0.00	0.00	1.38	0.91	0.77	0.36	1.51	34.56	0.28	1.83	1.15	1.09	1.04
	13	PM + 140	740		0.76		0.00	0.00	0.90	0.92	0.75	0.34	0.98	32.65	0.29	1.65	1.15	1.18	0.95
	14	PM + 130	730		0.70		0.00	0.00	1.11	0.87	1.10	0.28	1.27	30.94	0.54	1.20	1.10	1.02	0.94
	15	PM + 20	620		0.73		0.00	0.00	0.86	0.87	0.89	0.31	1.00	31.45	0.43	1.13	1.09	1.14	0.93
	16	GC-40	560		0.77		0.00	0.00	0.69	0.99	0.68	0.14	0.70	35.60	0.17	1.79	1.16	1.55	1.03
	17	GC-120	480		0.74		0.00	0.00	0.54	0.94	0.73	0.21	0.57	37.74	0.15	1.76	1.22	1.45	1.04
	18	GC-180	420		0.68		0.00	0.00	0.56	0.93	0.80	0.16	0.61	35.81	0.17	1.49	1.15	1.56	0.98
	19	GC-240	360		0.79		0.00	0.00	0.55	0.98	0.65	0.14	0.56	37.34	0.12	2.08	1.17	1.37	1.04
	20	GC-340	260		0.72		0.00	0.00	0.69	0.83	0.88	0.17	0.83	35.65	0.17	1.63	1.19	1.46	1.02
	21	GC-400	200		0.72		0.00	0.00	0.67	0.81	0.94	0.30	0.84	35.72	0.22	1.51	1.14	1.33	0.99
	22	GC-460	140		0.69		0.00	0.00	0.85	0.78	0.79	0.22	1.08	35.32	0.19	1.49	1.09	1.43	0.94
	23	GC-520	80		0.68		0.00	0.00	0.62	0.90	0.68	0.22	0.68	34.02	0.29	1.42	1.12	1.24	0.94
	24	GC-600	0		0.67		0.00	0.00	0.76	0.76	0.92	0.19	1.01	34.91	0.22	1.45	1.12	1.32	0.95

complexation model performs best in oxic–anoxic transition zones (Cao et al., 2022). The following relationship between trivalent Ce and dissolved oxygen/phosphate/pH show best consistency between model predicted Ce concentration and measurements, and are thereby applied to calculate our model results: $C_{Ce}\ \frac{1}{\{pO_2\}^{\frac{1}{4}}}; C_{Ce}\ (PO_4^{3-});\ C_{Ce}\ \{H^+\}^3$. To isolate the effect of redox conditions, the Ce anomaly is calculated using Nd and Pr, which counteracts the influence of phosphate variations, as these elements have similar complexation constants (Liu and Byrne, 1997; Luo and Byrne, 2004). From a thermodynamic perspective, while pH influences both Ce complexation and oxidation, the absolute Ce anomaly value is predominantly controlled by the oxidation of trivalent cerium, especially in suboxic to oxic environments. This process is exemplified by the Black Sea profile, where a minor pH increase (<0.2) corresponds to a significant rise in the Ce anomaly (0.1–0.9) associated with deoxygenation (German et al., 1991; Kondratiev et al., 2017).

3. Results

3.1. Ce anomaly records

The Ce/Ce* profiles in all seven study localities are plotted against their chemostratigraphy in Fig. 2. Across the examined intervals, the Ce/Ce* values ranged from 0.5 to 0.8 at Eastbourne (n = 23), 0.5 to 1.1 at Clot Chevalier (n = 12), and 0.8 to 1.7 at Raia del Pedale (n = 12). At Eastbourne, the Ce anomaly increases from 0.67 to 0.8 prior to the positive $\delta^{13}C$ excursion, subsequently decreasing shortly after its onset and returning to 0.55 (Fig. 2a). The overall Ce anomaly values indicate that Eastbourne maintained an oxic environment across the OAE 2 interval. Lu et al. (2010) also reported high-resolution Ce anomaly data (Ce anomaly = $\log[3Ce_n/(2La_n + Nd_n)]$, n means normalization of PAAS values) for Eastbourne, showing considerable detail through OAE 2. A comparison between the Ce anomaly from this study and that of Lu et al. (2010) is provided in the discussion. At Clot Chevalier, Ce/Ce* exhibits a rapid positive shift at the onset level of OAE 2, followed by a slow recovery throughout the event interval. At Raia del Pedale, the Ce/Ce* value exceeds 1 at the peak of the positive shift, with all values remaining above 0.8.

The OAE 2 interval is less well constrained by carbon-isotope profiles in the southern hemisphere. This study provides long-term Ce anomaly data for the Late Cretaceous Indian Ocean at a coarser resolution. At Hole 763B, Ce/Ce* values shifted from 1.3 to 0.3 (n = 39) starting at around the upper Albian–lower Cenomanian transition. A continuous decrease in Ce/Ce* is observed from the upper Cenomanian to middle Turonian interval, followed by values with low variability over the upper Turonian to lower Campanian interval. Ce/Ce* values at Hole 765C (n = 16) generally decrease over the Turonian interval with a few higher values (0.8) in the upper Cenomanian. The Turonian is characterized by lower Ce/Ce* (0.3). At Hole 766A, Ce/Ce* values (n = 32) gradually increase in the upper Cenomanian and peak near the boundary with the Turonian. In higher stratigraphic levels extending into the Campanian, Ce/Ce* values drop below 0.5. The Ce/Ce* record from Hole 1138A (n = 21) is similar to that of Hole 765C, decreasing from the upper Cenomanian to the lower Turonian then maintaining values

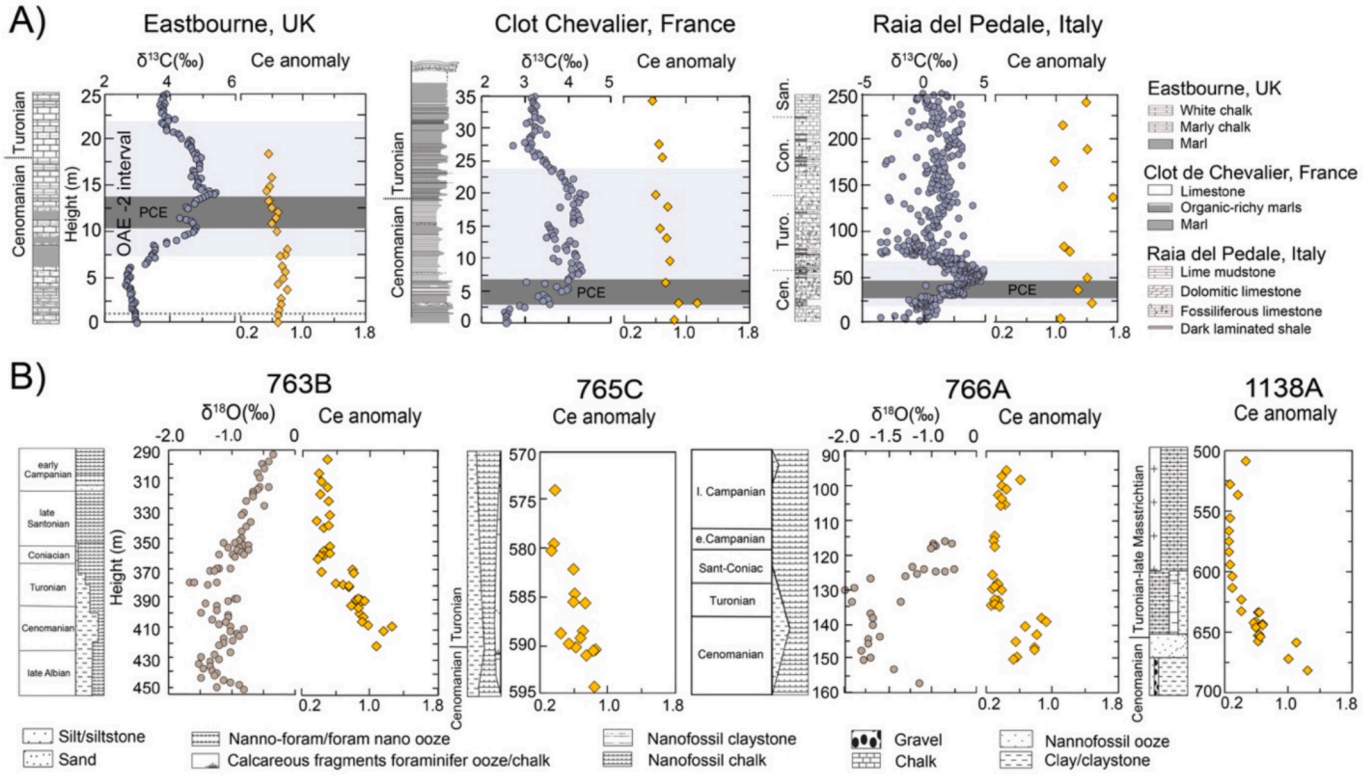

Fig. 2. Detailed chemostratigraphic plots for OAE 2 with Panel A documenting carbon- isotope and Ce/Ce* values at Eastbourne, UK; Clot Chevalier, France; Raia del Pedale, Italy. The stratigraphic columns for Eastbourne, Clot Chevalier and Raia del Pedale are from Owens et al. (2013); Panel B shows oxygen isotopes and Ce/Ce* values in samples from ODP/IODP Holes 763B, 765C, 766C and 1138A. Lithostratigraphy for the ODP holes and Cenomanian–Turonian boundary are compiled from ODP/IODP publications: 763B (Haq et al., 1991); 765C (Ludden and Gradstein, 1990b); 766A (Ludden and Gradstein, 1990a) and 1138A (Coffin et al., 2000; Dickson et al., 2017). Oxygen isotopes from ODP Holes 763B and 766A are from Clarke and Jenkyns (1999). The Ce anomaly data are generated in this study, and OAE 2 is marked by the area in light gray, as delineated by the positive $\delta^{13}C$ excursion (Keller et al., 2001; Tsikos et al., 2004; Owens et al., 2013; Gale et al., 2019). The dark gray band marks the Plenus Cold Event (PCE). The Plenus Cold Event was initially proposed for the European Chalk Sea based on southward invasion of boreal faunas (Gale and Christensen, 1996; Keller et al., 2004; Forster et al., 2007; O'Connor et al., 2020). Gray dashed line (only at Eastbourne) represents the onset of the Ce/Ce* value shift.

around 0.3 for the higher parts of the Cretaceous, extending into the Maastrichtian. In summary, Ce/Ce* values predominantly decreased starting from the upper Cenomanian at ODP/IODP holes in the southern Indian Ocean except for 766A. The Ce anomaly gradually increased from 0.5 to 1.0 before the Cenomanian-Turonian boundary. Post-boundary Ce anomaly values are consistently between 0.3 and 0.5 across all southern Indian Ocean sites.

3.2. Model results

The modeled results, calculated relative to pre-OAE Ce anomaly baselines of 0.67 for Eastbourne, 0.84 for Clot Chevalier, and 1.0 for Raia del Pedale, indicate a maximum dissolved oxygen loss of 50 %, 70 %, and 85 % in the upper water column at these respective sites (Fig. 3). For the proto-Indian Ocean, only ODP Hole 766A was modeled due to its recorded increase in Ce anomaly across the Cenomanian-Turonian boundary. Because the Ce anomaly's sensitivity to dissolved oxygen diminishes in more oxic conditions, the calculated oxygen increase for the post-OAE period carries large uncertainties and is therefore not discussed here. Absolute Ce anomaly values are used as indicators of oxygenation in oxidized environments.

4. Discussion

We first evaluate the fidelity of the Ce-anomaly data, considering potential contamination from secondary phases and diagenetic alteration. Next, we assess spatial redox heterogeneity by comparing the Ce anomalies with other redox proxies. We then explore the driving mechanisms of OAE 2 and the timing of deoxygenation. Finally, we analyze the modeling results and their global implications for modern ocean deoxygenation.

4.1. Fidelity of the Ce-anomaly data

Potential contamination of the carbonate Ce anomaly mainly comes from the adsorbed REE on clay and Mn-oxides as well as structural REY in clay and silicate minerals. REY in possible minerals contaminants usually exhibit no or positive Ce anomalies (Cao et al., 2020). This study adopts a verified sequential leaching protocol that extracts REY signals in carbonate minerals while eliminating contamination from non-carbonate phases such as Mn-oxides, clay and silicate minerals (Cao et al., 2020, 2023). Three leaching steps using ammonium acetate and ammonium carbonate effectively remove the adsorbed REE because they are weekly bonded. Elemental ratios are used to further evaluate the robustness of Ce anomaly data and those showing evidence of contamination are excluded. Al and Rb are not enriched in limestone but are more abundant in clay and silicates as structural and adsorbed phases. We use Al/Ca $<$ 1.2 mmol/mol and Rb/Sr $<$ 1 mmol/mol as screening criteria to indicate no dissolution of clay and silicate minerals (Pogge von Strandmann et al., 2013; Cao et al., 2023; Liu et al., 2013). A few samples have Al/Ca and Rb/Sr values that are slightly higher than our filtration criteria (Fig. 4). However, they show negative Ce anomalies and the values are similar to those of the neighbouring samples in the depth profile (Table 1). Typical Mn nodule (NOD-A-1) has Mn/Ca around 0.5 mol/mol, and Fe/Ca 0.3 mol/mol. Based on the mass balances, if dissolved Fe/Mn oxides were to take up 1 % of the total mass this would result in Mn/Ca of 5 mmol/mol and Fe/Ca ratio of 3 mol/mol of the leachate. The leaching method applied in this study can be applied to samples containing 1 % of Mn/Fe oxides (Cao et al., 2020). Mn/Ca of all samples is lower than 4.5 mmol/mol and Fe/Ca is lower than 3 mmol/mol with two outliers. No positive correlations are observed between the Ce anomaly and Mn/Ca as well as Ce anomaly and Fe/Ca, implying no or minimal influence from Fe/Mn oxides and hydroxides. Total REY/Ca ratios are lower than 1.0 ug/g, which values are comparable to those observed in calcite precipitation experiments (Voigt et al., 2004), indicating an absence of REY signal from non-carbonate minerals. Although burial dolomitization and meteoric-water alteration have limited influence on the REY patterns (Banner et al., 1988; Webb and Kamber, 2000; Bargar et al., 2009; Liu et al., 2019), we filtered out a few samples with significantly higher Mg/Ca ratios (60 mmol/mol to 200 mmol/mol). Mn/Sr ratios of all samples are lower than 3 mol/mol, indicating no diagenetic overprint (Kaufman et al., 1993). Therefore, the Ce anomaly data of these samples are still considered valid. Finally, a lack of correlation between the Ce anomaly and various elemental ratios further confirms that the Ce anomaly data represent primary signals of seawater and are not contaminated by clay, silicates and Fe-Mn oxyhydroxides (Fig. 4).

4.2. Spatial variability in oceanic redox responses to OAE 2

For Eastbourne, a comparison of our Ce anomaly data in this study with the record by Lu et al. (2010) reveals broadly consistent trends (Fig. 5A). Although the absolute values are not directly comparable due to differing calculation methods—$\log[3Ce_n/(2La_n + Nd_n)]$ in Lu et al. (2010) versus $Ce_n/(Pr_n(Pr_n/Nd_n))$ in this study—both profiles show a decrease in the Ce anomaly coincident with the positive carbon-isotope excursion (CIE) that marks the onset and duration of OAE 2. Our Ce/Ce* values, ranging from 0.5 to 0.8, agree well with the values from −0.5 to −0.1 reported by Lu et al. (2010), suggesting that oxic conditions persisted in the upper ocean throughout the OAE 2 interval. The two positive Ce/Ce* excursions indicate two episodes of deoxygenation (or a phase of oxygenation within an overall episode of deoxygenation), which is consistent with the two-phase negative shifts in iodine/calcium ratios (Lu et al., 2010; Zhou et al., 2015). The intervening excursion to lower Ce/Ce* and higher I/Ca likely records a transient local watermass that was relatively more oxygenated, which may be related to the Plenus Cold Event (Owens et al., 2013; Jenkyns et al., 2017; Clarkson et al., 2018; O'Connor et al., 2020).The Ce anomaly in this study exhibits no discernible response to this event probably due to courser sampling/analysis resolution.

A similar decreasing trend in the Ce anomaly across the CIE is also observed at Clot Chevalier. The peak Ce anomaly values (1.0–1.8) occur at the onset of OAE 2, suggesting conditions were briefly anoxic before reoxygenation during the remainder of the event. This interpretation is consistent with the relatively degraded nature of the organic matter in this section (Gale et al., 2019). By contrast, all Ce/Ce* values from Raia del Pedale exceed 1.0, pointing to a more persistently reducing environment than at Eastbourne. This interpretation aligns with the I/Ca record, which remains consistently low at ~1–2 μmol/mol throughout the section, indicating that the local near-surface waters were relatively oxygen-depleted (Zhou et al., 2015). Immediately above the falling limb of the $\delta^{13}C$ excursion (post-OAE 2) at Raia del Pedale, I/Ca values average 1.2 umol/mol, values that are lower than those found at Eastbourne at the same stratigraphic level (Zhou et al., 2015). Notably, this section was likely deposited in a shallower water setting compared to Eastbourne, yet exhibits stronger evidence for deoxygenation.

For the proto-Indian ocean, Hole 766A records an increase in the Ce anomaly from 0.83 to 1.0 prior to the Cenomanian–Turonian boundary. By contrast, the other three sites (763B, 765C, 1138A) show a general decreasing trend in Ce/Ce* values post-dating the upper Cenomanian, with consistently lower Ce/Ce* values of ~0.4 following the stage boundary with the Turonian (Fig. 2). While a few samples in the bottom of the 763B and 1138A sections show Ce anomalies higher than 1.0 such values do not represent a sustained trend. These trends can be contextualized within the long-term climatic evolution. $\delta 1^8O$ data from ODP Holes 763 and 766 indicate a general warming trend through the Albian and Cenomanian into the early Turonian (Clarke and Jenkyns, 1999; Falzoni et al., 2016a), a global pattern of climatic evolution (Friedrich et al., 2012; O'Brien et al., 2017; Robinson et al., 2019). This interval of Late Cretaceous warming corresponds to higher Ce/Ce*, whereas the subsequent cooling, which continued at a slower rate through the late Campanian and Maastrichtian (O'Brien et al., 2017), is marked by

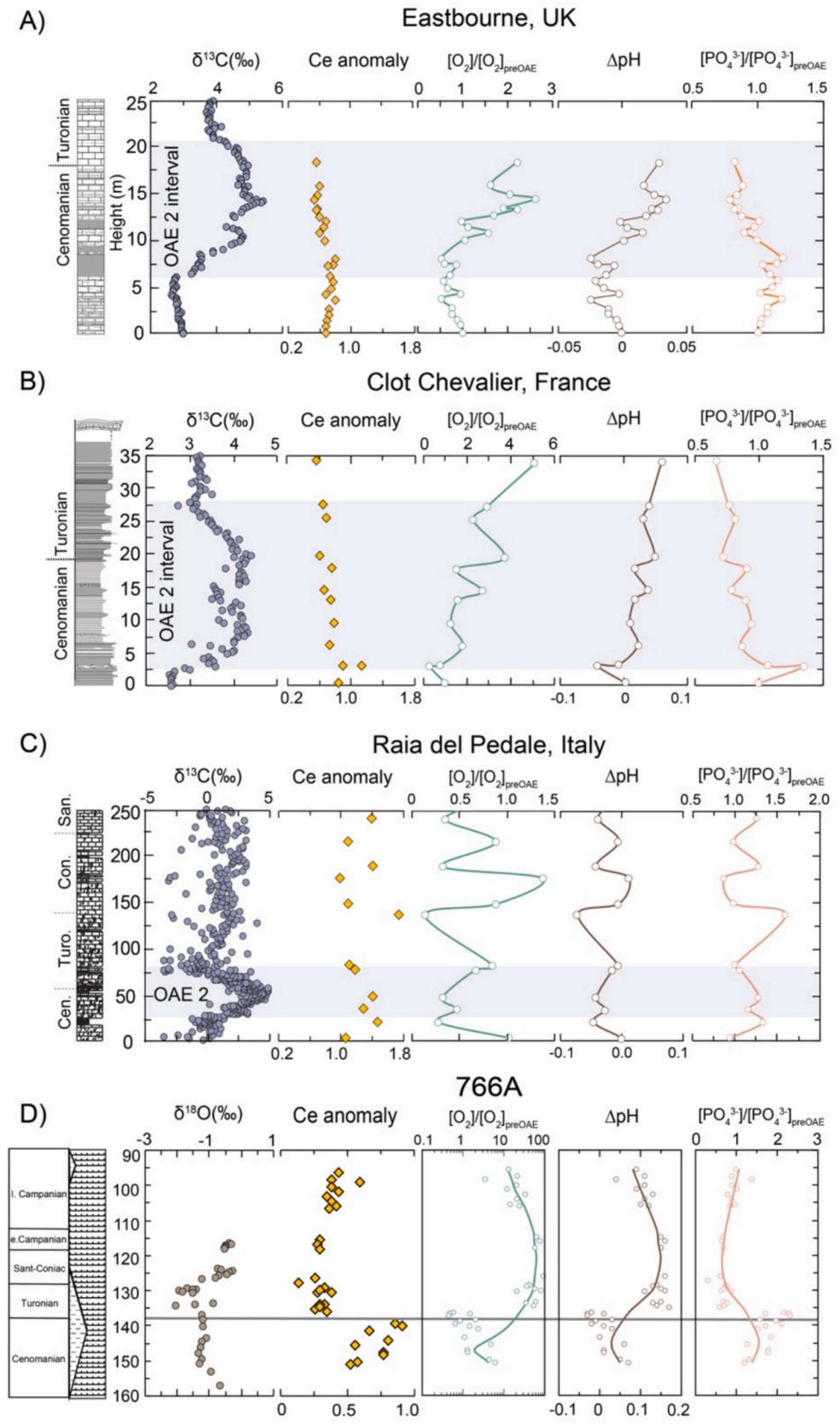

Fig. 3. Modeling changes of oceanic dissolved oxygen, pH and phosphate concentrations. Dissolved oxygen change (O_2/post-OAE 2) is expressed as a ratio of dissolved oxygen compared to pre-OAE 2; pH change (ΔpH) is expressed as $pH_t - pH_{pre\text{-}OAE\ 2}$. Phosphate concentration change is also expressed in a ratio of phosphate compared to pre-OAE 2 values.

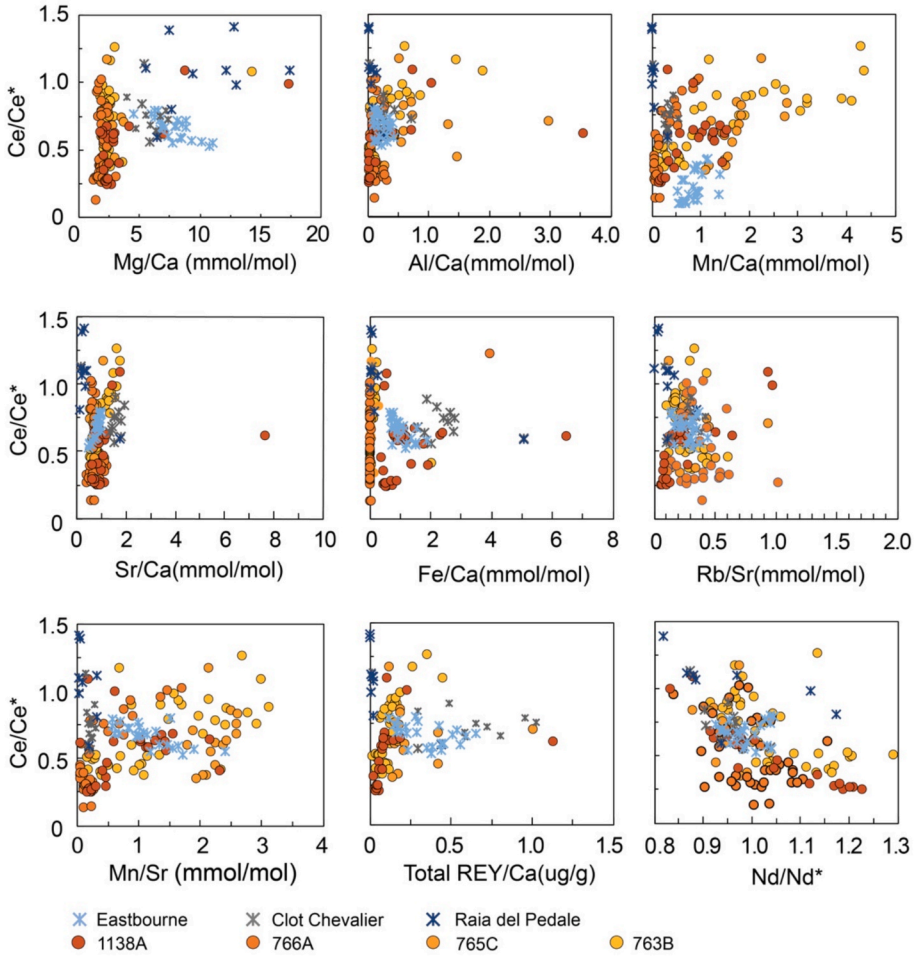

Fig. 4. A comparison of REY with major- and trace-element alteration proxies for sequentially leached samples.

relatively low Ce/Ce* values.

Synthesizing these records, the increase in the Ce anomaly during the Late Cretaceous across all study sites indicates that upper ocean deoxygenation was a widespread phenomenon. However, the presence of anoxia-indicative Ce anomaly values (>1.0) are only observed at Clot Chevalier, Raia del Pedale, and Hole 763B suggests that intense oxygen depletion was likely restricted to specific paleo-environmental settings, rather than being ubiquitous. This spatial heterogeneity can be explained by the balance between competing mechanisms. High oxygen consumption via biotic respiration in the upper ocean would drive net oxygen loss. Conversely, the increased burial of organic carbon during most of OAE 2 (excluding the Plenus Cold Event) would have released oxygen into the ocean–atmosphere system, potentially ventilating various environments (Newby et al., 2025). The dominant negative trend in Ce/Ce* observed during OAE 2 at many sites is consistent with the latter process of enhanced ventilation from organic-carbon burial (Boudinot et al., 2020). However, the initial increase in Ce/Ce* during the early stages of the positive $\delta^{13}C$ excursion suggests that respiration rates initially outpaced this oxygen supply, leading to net deoxygenation. This elevated oxygen consumption could be attributed to multiple factors, including CO_2 effects on marine organisms and ecosystems, changes in the quality of sinking particles, and increased nutrient supply from the ocean interior or continents. Support for the nutrient supply hypothesis comes from relatively light $\delta^{7}Li$ signatures in several OAE 2 sections, which suggest an increase in both the rate and intensity of silicate weathering in subaerial and marine realms (Pogge von Strandmann et al., 2013). Such enhanced weathering would have stimulated nutrient supply, thereby fuelling planktonic productivity and, consequently, oxygen consumption in the upper water column.

4.3. Deoxygenation timing

The Cenomanian–Turonian $\delta^{13}C$ curve acts as both a stratigraphic marker and as a monitor of global marine organic-carbon burial with its first (stratigraphically lowest) positive shift conventionally taken as defining the onset of OAE 2 (e.g. Jenkyns et al., 2017). Within the Eastbourne chalk section, both our data and the ones from Lu et al. (2010) show an increasing Ce anomaly in the pre-OAE interval alongside relatively low I/Ca ratios. This finding, supported by high pre-OAE nannofossil and dinocyst fertility indices (Pearce et al., 2009), implies that, at least regionally, deoxygenation occurred before the global carbon-cycle perturbation typically used to define the OAE (Jenkyns, 2010). This phenomenon is equally suggested by a global drawdown of vanadium in an equatorial Atlantic ODP site (Demerara Rise) that began ~75 kyr prior to the onset of OAE 2, which itself coincided with a drop in molybdenum content: phenomena that illustrate the differential expansion of anoxia and euxina in the water column (Owens et al., 2016b). Similarly, Ostrander et al. (2017), based on Tl-isotope records from the same ODP site, have calculated that deoxygenation at the sediment–water interface expanded ~43 kyr before the globally recognized carbon-cycle perturbation of OAE 2. In addition, nitrogen isotopes suggest that the transition from oxia to anoxia took place locally (Tarfaya, Morocco) even earlier in an area of persistent upwelling (Scholz et al., 2019). Hence, the redox conditions that characterized OAE 2 began to develop well before its onset, as conventionally described by the initial rise in carbon-isotope values. Previous global records cannot

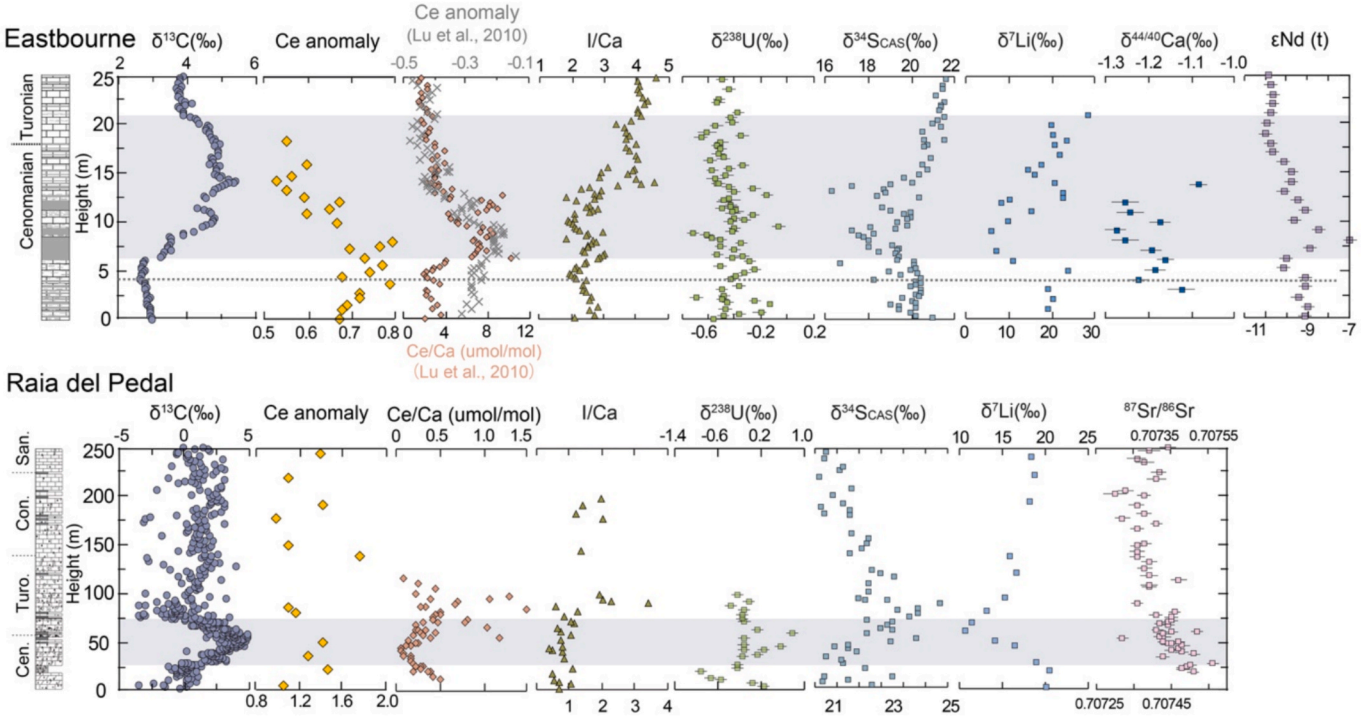

Fig. 5. Geochemical data compilation for Eastbourne and Raia del Pedale. Ce anomaly data compared with other redox proxies are I/Ca ratios (Lu et al., 2010; Zhou et al., 2015); $\delta^{238}U$ (Clarkson et al., 2018) and $\delta^{34}S_{CAS}$ values (Owens et al., 2013); weathering proxies including $\delta^{7}Li$, $^{87}Sr/^{86}Sr$ (Pogge Von Strandmann et al., 2013) and $\delta^{44/40}Ca$ (Blättler et al., 2011; Du Vivier et al., 2015); and Nd isotopes that are used to constrain oceanic circulation and hydrothermal activity (Zheng et al., 2013). Ce/Ca ratios are taken from Lu et al. (2010). The gray area marks the OAE 2 interval as defined by the $\delta^{13}C$ profile. The dashed line in the Eastbourne graph marks the initiation of deoxygenation at this locality according to redox proxy data; this point in time, as represented by this line, manifestly preceded OAE 2, as conventionally fixed by the initial rise in carbon-isotope values.

provide local heterogeneous data. Thus, Ce provide evidence for significant spatial heterogeneity in oceanic responses driven by regional oceanographic processes. While Eastbourne and Demerara Rise clearly record pre-OAE oxygen loss, other sections do not show signals of early deoxygenation, likely reflecting differences in ocean circulation patterns and nutrient supply. For instance, regions influenced by enhanced upwelling or restricted water mass circulation may have experienced more rapid and pronounced oxygen depletion prior to the carbon-isotope excursion, whereas well-ventilated open-ocean settings could have maintained oxic environment until the full onset of OAE 2.

We posit that the OAE 2 event was initiated by a pulse of nutrient delivery—potentially from enhanced hydrothermal fluxes or climatically accelerated weathering—which spurred a primary productivity increase (Nana Yobo et al., 2021; Turgeon et al., 2008; Pogge von Strabdmann et al., 2013). The shifts in radiogenic osmium isotopes and Li isotopes occur before or at the onset of the positive carbonate-isotope excursion. This time lag varies from 60 kyr in Iona-1 core in Texas, 23 kyr in ODP site 1206B, 30 kyr in Eastbourne, while no time lag is observed in Raia del Pedale (Nana Yobo et al., 2021; Turgeon et al., 2008; Pogge von Strabdmann et al., 2013). Subsequently, enhanced preservation of organic matter under low-oxygen, high-sedimentation conditions, particularly in marginal settings like epeiric seaways and coastal upwelling zones, became the dominant feedback, driving the positive carbon-isotope excursion. The massive burial of organic carbon drew down atmospheric CO_2, leading to climatic cooling. Concurrently, the generally more reducing ocean decreased the inventories of fixed nitrogen and bio-essential trace metals, thereby suppressing the high productivity that had helped initiate the event. These negative feedbacks, operating alongside the limited spatial extent of toxic euxinia, gradually returned the ocean to more oxidizing conditions. This chain of events, where an initial perturbation is amplified and then terminated by its own consequences, may represent a recurring pattern in the history of Phanerozoic oceanic anoxia. This spatial variability in redox responses underscores the importance of local to regional oceanographic conditions in modulating the timing and intensity of deoxygenation, even within the context of a globally synchronous carbon- cycle perturbation.

4.4. *Implications for oceanic deoxygenation events*

Oceanic deoxygenation events, characterized by significant declines in dissolved oxygen levels in seawater, have occurred repeatedly over geological history and are now being exacerbated by human activities. Deoxygenation in the ocean interior results from an imbalance of oxygen supply and consumption (Keeling et al., 2010; Levin, 2018; Oschlies et al., 2018). Warming is considered the main driver for surface-water oxygen decline because oxygen solubility decreases with increasing ocean temperature. For example, seawater warming from 10 °C to 30 °C leads to a 30 % loss in oxygen solubility (Kester, 1975). For the three European sites, both average and maximum Ce/Ce* values during OAE 2 increase towards lower latitudes and might have been resulted from a local temperature response (Fig. 7). However, such a spatial heterogeneity is not shown in any of the four ODP/IODP holes in the proto-Indian Ocean. OAE 2 is assumed to represent a hyperthermal within the overall context of a CO_2-inspired greenhouse climate with relatively elevated sea-surface temperatures, in excess of 35 °C, at low latitudes (Huber et al., 2002; Forster et al., 2007; Adams et al., 2010; Barclay et al., 2010; Friedrich et al., 2012, 2006 ; O'Brien et al., 2017; Robinson et al., 2019). However, ocean warming alone cannot completely explain the different redox evolution patterns between the Atlantic Ocean and the Indian Ocean. Our model calculated more than 30 % decrease in dissolved oxygen, suggesting other controlling factors besides solubility. The distribution of oxygen in the upper water column is affected by the downwelling of oxygen-rich surface water, and upwelling of oxygen-

poor waters. Sluggish ocean circulation, or overturning associated with tropical deep-water formation, could have substantially reduced the supply of oxygen in the ocean below the surface saturation zone. For example, Brass et al. (1982) introduced the WSBW (warm saline bottom water) hypothesis, in which increased evaporation in the tropical shelf areas produced very warm dense brines that sank to form deep water instead of the cold and relatively salty water currently downwelling at high latitudes. Trabucho Alexandre et al. (2010) supported this hypothesis and further suggested an estuarine circulation between the North Atlantic and Pacific Oceans during the mid-Cretaceous. Such Pacific-derived nutrient-rich deep water would have been depleted in dissolved oxygen due to its decreased solubility in warm water and, where locally upwelled in the Atlantic and surrounding areas, favored high productivity and the deposition of organic-rich sediments, particularly during OAEs. Such a mechanism may have been responsible for significant anoxia, even in waters of modest depth such as characterized Raia del Pedale during OAE 2. Significantly, evidence for intermittent low-oxygen conditions in this section around Cenomanian–Turonian boundary time is found in the local development of black microbially laminated carbonates with total organic carbon (TOC) contents up to 1 % (Frijia et al., 2019). By contrast, Eastbourne was not greatly affected by an anoxic upper water column at this time due to its higher latitude, different oceanographic setting and ocean circulation, at times bringing Arctic waters to the region. This paleoceanographic model is supported by a positive εNd excursion at this site, which was likely due to the transport of radiogenic Nd from a volcanic source, most likely the High Arctic LIP via boreal seawater, or Caribbean LIP via other routes (Fig. 5) (Zheng et al., 2013). Because Eastbourne has relatively low Ce/Ce* values over the OAE 2 interval, it is unlikely that this area received waters from the Pacific at this time because they would have been more depleted in oxygen. A Nd-isotope (εNd) shift recorded at intermediate-water depths (site 763), but not at deep-water locations (site 765 and 766) in the proto-Indian Ocean during the late Cenomanian–early Turonian interval indicates that the proto-Indian Ocean was actively ventilated (Thomas and Tilghman, 2014) (Fig. 6). Thus, the accumulation and burial of anomalously high amounts of organic carbon in seafloor sediments in this area during OAE 2 has been attributed to enhanced surface-water productivity and high carbon flux to the seafloor, instead of diminished bottom-water ventilation (Thomas and Tilghman, 2014).

5. Conclusions

The Ce anomaly in ancient marine carbonates serves as a powerful paleo-redox tracer, revealing that the Cenomanian–Turonian Oceanic Anoxic Event 2 (OAE 2) was not a monolithic, globally uniform phenomenon, but rather a complex mosaic of spatially and temporally heterogeneous redox conditions. However, extreme anoxia was restricted to ocean basins where high oxygen demand was met with low oxygen supply from diffusion and ocean circulation, locally even in relatively shallow-water areas. The Ce-anomaly records from northern and southern Europe and the proto-Indian Ocean reveal redox conditions in the upper ocean during OAE 2 that were geographically distinctive and dynamic. The timing of deoxygenation in the upper ocean was not uniform, and some sites predated the positive change in the carbon-isotope signature used to define the onset of OAE 2 at Eastbourne, a phenomenon already indicated by previously published trace-element data, as well as vanadium and thallium isotope data. A progressive increase in the average Ce anomaly in three European sites situated at progressively lower latitudes in the Northern Hemisphere is

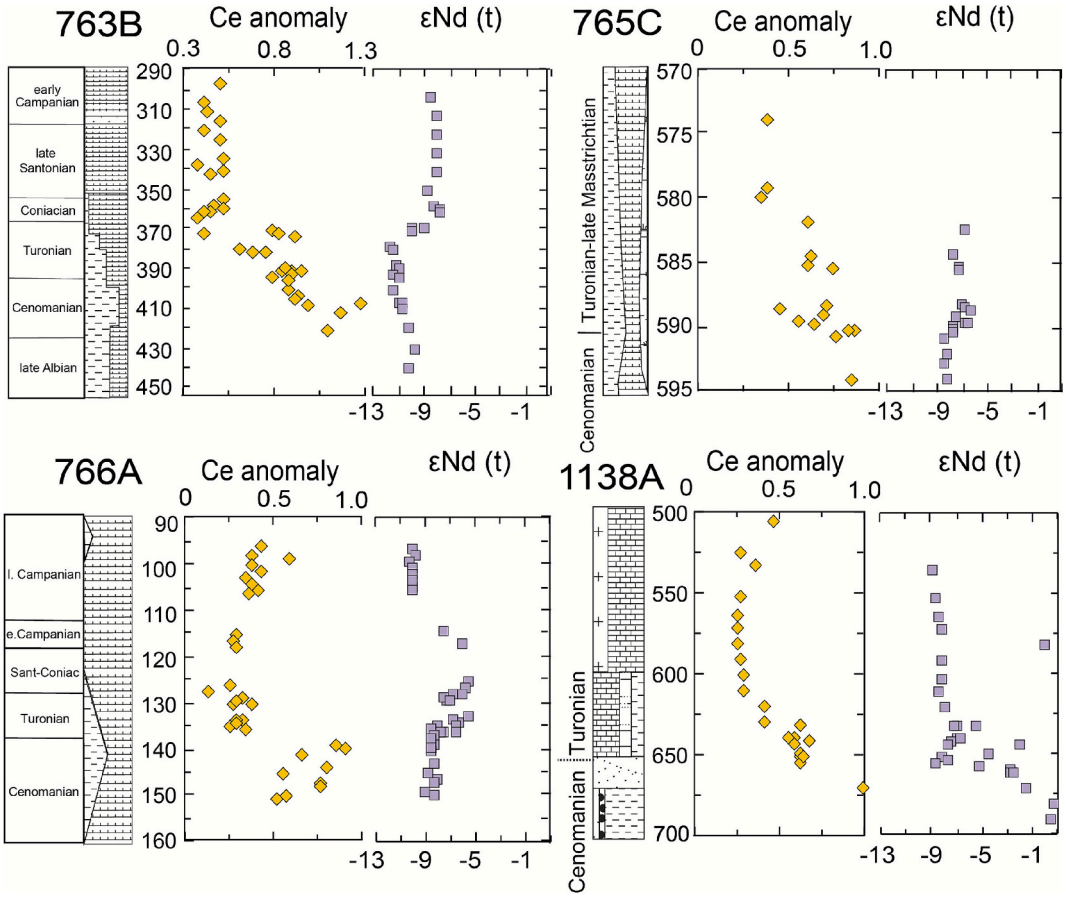

Fig. 6. Geochemical data compilation for ODP sites in the southern Indian Ocean. Nd isotopes are replotted against sediment depth, and depths for each sample are compiled from Martin et al. (2010) and Thomas and Tilghman (2014), as well as calculated using ODP core summary database.

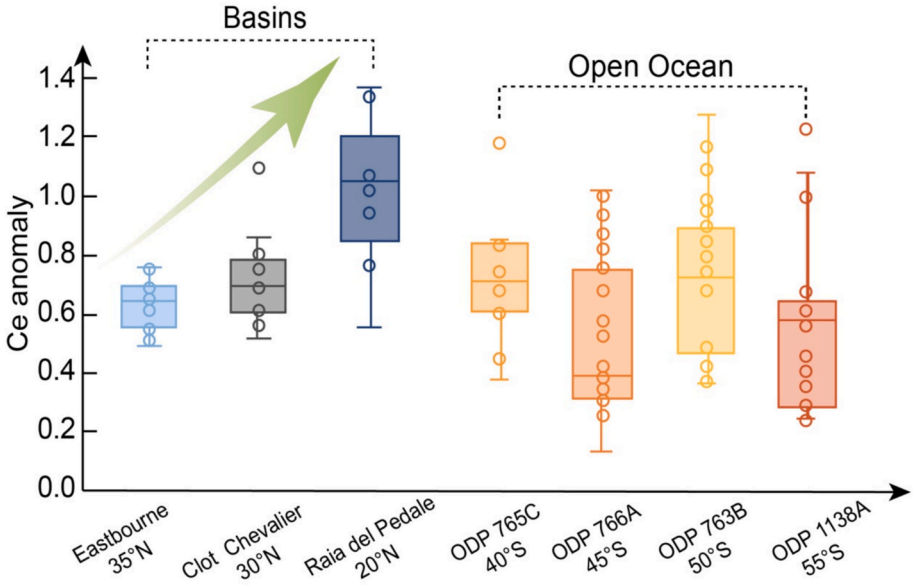

Fig. 7. Box and whisker plots of Ce/Ce* values in each site. Estimated paleolatitudes for each section and ODP holes are based on Haq et al. (1992); Martin et al. (2010); Robinson et al. (2010); Owens et al. (2013); Gale et al. (2019).

consistent with an overturning in the North Atlantic Ocean and surrounding seas during OAE 2. Local redox variations, particularly if manifested as extreme anoxia, were likely influenced by different factors including continental weathering and nutrient supply, upwelling, planktonic productivity, ocean circulation, water mass stratification, and thermocline depth. The overall decreasing Ce/Ce* after the onset of OAE 2 in late Cenomanian and subsequent stages indicates reoxygenation in the upper ocean, possibly driven by global organic-matter burial, causing oxygen release to the ocean–atmosphere system. Significantly lower Ce/Ce* values through the late Turonian into the Maastrichtian suggest that the upper ocean recovered to a fully oxidized state, likely driven by negative feedbacks. Enhanced organic-carbon burial, which drove the $\delta^{13}C$ excursion, would have drawn down atmospheric CO_2, leading to climatic cooling and a reduction in nutrient supply from weathering. To fully resolve this global redox mosaic, complementary high-resolution records from under-sampled basins, particularly the Pacific, are essential to test the interplay between ocean circulation, nutrient dynamics, and climate in shaping one of the most significant perturbations in Earth's history.

CRediT authorship contribution statement

Cheng Cao: Writing – review & editing, Writing – original draft, Visualization, Validation, Resources, Project administration, Methodology, Investigation, Funding acquisition, Formal analysis, Data curation, Conceptualization. **Xiao-Ming Liu:** Writing – review & editing, Validation, Resources, Project administration, Conceptualization. **Jeremy D. Owens:** Writing – review & editing, Validation, Resources. **Hugh C. Jenkyns:** Writing – review & editing, Validation.

Data availability

Data are available at Mendeley data https://doi.org/10.17632/3vf8n9bjyc.1.

Declaration of competing interest

The authors declare that they have no known competing financial interests or personal relationships that could have appeared to influence the work reported in this paper.

Acknowledgments

We thank Debbie Thomas for sample contribution and Tim Lyons for helpful discussion. CC acknowledges the funding support from National Key Research and Development Program of China (2024YFF0807602) and Fundamental Research Funds for the Central Universities (0206/14380232) at Nanjing University. JDO acknowledges support from the National High Magnetic Field Laboratory. X-ML acknowledges William F. McDonough, whose critical thinking and curiosity about the Earth's interior and its evolution have shaped the way X-ML approaches scientific problems. This article forms part of the *GCA* McDonough Special Issue, "Geochemical Insights into Planetary Evolution: from Core to Surface," celebrating his distinguished career.

References

Adams, D.D., Hurtgen, M.T., Sageman, B.B., 2010. Volcanic triggering of a biogeochemical cascade during Oceanic Anoxic Event 2. Nat. Geosci. 3, 201–204.
Arthur, M.A., Schlanger, S.O., Jenkyns, H.C., 1987. The Cenomanian-Turonian Oceanic Anoxic Event, II. Palaeoceanographic controls on organic-matter production and preservation. Geol. Soc. London, Spec. Publ. 26, 401–420.
Arthur, M.A., Brumsack, H.-J., Jenkyns, H.C., Schlanger, S.O., 1990. Stratigraphy, geochemistry, and paleoceanography of organic carbon-rich cretaceous sequences. In: Ginsburg, R.N., Beaudoin, B. (Eds.), Cretaceous Resources, Events and Rhythms. Springer, Netherlands, Dordrecht, pp. 75–119.
Bach, W., Irber, W., 1998. Rare earth element mobility in the oceanic lower sheeted dyke complex: evidence from geochemical data and leaching experiments. Chem. Geol. 151, 309–326.
Banner, J.L., Hanson, G.N., Meyers, W.J., 1988. Rare earth elements and Nd isotopic variations in regionally extensive dolomites from the Burlington-Keokuk formation (Mississippian) : implications for REE mobility during carbonate diagenesi. J. Sediment. Petrol. 58, 415–432.
Barclay, R.S., McElwain, J.C., Sageman, B.B., 2010. Carbon sequestration activated by a volcanic CO2 pulse during Ocean Anoxic Event 2. Nat. Geosci. 3, 205–208.
Bargar, J.R., Fuller, C.C., Marcus, M.A., Brearley, A.J., Perez De la Rosa, M., Webb, S.M., Caldwell, W.A., 2009. Structural characterization of terrestrial microbial Mn oxides from Pinal Creek. AZ. Geochim. Cosmochim. Acta 73, 889–910.
Blättler, C.L., Jenkyns, H.C., Reynard, L.M., Henderson, G.M., 2011. Significant increases in global weathering during Oceanic Anoxic Events 1a and 2 indicated by calcium isotopes. Earth Planet. Sci. Lett. 309, 77–88.
Blumenberg, M., Wiese, F., 2012. Imbalanced nutrients as triggers for black shale formation in a shallow shelf setting during the OAE 2 (Wunstorf, Germany). Biogeosciences 9, 4139–4153.
Bodin, S., Godet, A., Westermann, S., Föllmi, K.B., 2013. Secular change in northwestern Tethyan water-mass oxygenation during the late Hauterivian–early Aptian. Earth Planet. Sci. Lett. 374, 121–131.
Boudinot, F.G., Sepúlveda, J., 2020. Marine organic carbon burial increased forest fire frequency during Oceanic Anoxic Event 2. Nat. Geosci. 13, 693–698.

Brass, G., Southam, J., Peterson, W.H., 1982. Warm saline bottom water in the ancient ocean. Nature 296, 620–623.
Byrne, R.H., Bingler, L.S., 1989. Comment on "Cerium: A chemical tracer for paleo-oceanic redox conditions" by Y.-G. Liu, M. R. U. Miah and R. A. Schmitt. Geochim. Cosmochim. Acta.
Byrne, R.H., Lee, J.H., Bingler, L.S., 1991. Rare earth element complexation by PO_4^{3-} ions in aqueous solution. Geochim. Cosmochim. Acta 55, 2729–2735.
Cantrell, K.J., Byrne, R.H., 1987. Rare earth element complexation by carbonate and oxalate ions. Geochim. Cosmochim. Acta 51, 597–605.
Cao, C., Liu, X.-M., Bataille, C.P., Liu, C., 2020. What do Ce anomalies in marine carbonates really mean? a perspective from leaching experiments. Chem. Geol. 532, 119413.
Cao, C., Liu, X., Chen, J., 2022. Cerium anomaly as a tracer for paleo-oceanic redox conditions: a thermodynamics-based Ce oxidation modeling approach. Front. Earth Sci. 10, 1–13.
Cao, C., Liu, X.-M., Wang, X.-K., Chen, J., 2023. Effective use of limestones to reconstruct seawater Li isotope compositions - a community standard proposal. Chem. Geol. 626, 121441.
Clarke, L.J., Jenkyns, H.C., 1999. New oxygen isotope evidence for long-term cretaceous climatic change in the Southern Hemisphere. Geology 27, 699–702.
Clarkson, M.O., Stirling, C.H., Jenkyns, H.C., Dickson, A.J., Porcelli, D., Moy, C.M., Pogge von Strandmann, P.A.E., Cooke, I.R., Lenton, T.M., 2018. Uranium isotope evidence for two episodes of deoxygenation during Oceanic Anoxic Event 2. Proc. Natl. Acad. Sci. 115, 2918–2923.
Coffin, M.., Frey, F.A., Wallace, P.J., 2000. Shipboard Scientific Party, 2000. Site 1138, in: Proc. ODP, Init. Repts. College Station, TX (Ocean Drilling Program), pp. 1–205.
Damsté, J.S.S., Köster, J., 1998. A euxinic southern North Atlantic Ocean during the Cenomanian/Turonian oceanic anoxic event. Earth Planet. Sci. Lett. 158, 165–173.
Damsté, J.S.S., Elisabeth C. van Bentum, Gert-Jan Reichart, Jörg Pross, Stefan Schouten, 2010. A CO2 decrease-driven cooling and increased latitudinal temperature gradient during the mid-Cretaceous Oceanic Anoxic Event 2. Earth Planet. Sci. Lett. 293, 97–103.
Dickson, A.J., Saker-Clark, M., Jenkyns, H.C., Bottini, C., Erba, E., Russo, F., Gorbanenko, O., Naafs, B.D.A., Pancost, R.D., Robinson, S.A., van den Boorn, S.H.J., Idiz, E., 2017. A Southern Hemisphere record of global trace-metal drawdown and orbital modulation of organic-matter burial across the Cenomanian–Turonian boundary (Ocean Drilling Program Site 1138, Kerguelen Plateau). Sedimentology 64, 186–203.
Du Vivier, A.D.C., Jacobson, A.D., Lehn, G.O., Selby, D., Hurtgen, M.T., Sageman, B.B., 2015. Ca isotope stratigraphy across the Cenomanian-Turonian OAE 2: Links between volcanism, seawater geochemistry, and the carbonate fractionation factor. Earth Planet. Sci. Lett. 416, 121–131.
Du Vivier, A.D.C., Selby, D., Sageman, B.B., Jarvis, I., Gröcke, D.R., Voigt, S., 2014. Marine 187Os/188Os isotope stratigraphy reveals the interaction of volcanism and ocean circulation during Oceanic Anoxic Event 2. Earth Planet. Sci. Lett. 389, 23–33.
Eldrett, J.S., Ma, C., Bergman, S.C., Lutz, B., Gregory, F.J., Dodsworth, P., Phipps, M., Hardas, P., Minisini, D., Ozkan, A., Ramezani, J., Bowring, S.A., Kamo, S.L., Ferguson, K., Macaulay, C., Kelly, A.E., 2015. An astronomically calibrated stratigraphy of the Cenomanian, Turonian and earliest Coniacian from the cretaceous Western Interior Seaway, USA: Implications for global chronostratigraphy. Cretac. Res. 56, 316–344.
Falzoni, F., Petrizzo, M.R., Clarke, L.J., MacLeod, K.G., Jenkyns, H.C., 2016a. Long-term late cretaceous oxygen-and carbon isotope trends and planktonic foraminiferal turnover: a new record from the southern midlatitudes. Bull. Geol. Soc. Am. 128, 1725–1735.
Falzoni, F., Petrizzo, M.R., Jenkyns, H.C., Gale, A.S., Tsikos, H., 2016b. Planktonic foraminiferal biostratigraphy and assemblage composition across the Cenomanian-Turonian boundary interval at Clot Chevalier (Vocontian Basin, SE France). Cretac. Res. 59, 69–97.
Forster, A., Schouten, S., Moriya, K., Wilson, P.A., Damsté, J.S.S., 2007. Tropical warming and intermittent cooling during the Cenomanian/Turonian oceanic anoxic event 2: Sea surface temperature records from the equatorial Atlantic. Paleoceanography 22, 1–14.
Frey, F.A., Coffin, M.F., Wallace, P.J., Weis, D., Zhao, X., Wise, S.W., Wähnert, V., Teagle, D.A.H., Saccocia, P.J., Reusch, D.N., Pringle, M.S., Nicolaysen, K.E., Neal, C. R., Müller, R.D., Moore, C.L., Mahoney, J.J., Keszthelyi, L., Inokuchi, H., Duncan, R. A., Delius, H., Damuth, J.E., Damasceno, D., Coxall, H.K., Borre, M.K., Boehm, F., Barling, J., Arndt, N.T., Antretter, M., 2000. Origin and evolution of a submarine large igneous province: the Kerguelen Plateau and Broken Ridge, southern Indian Ocean. Earth Planet. Sci. Lett. 176, 73–89.
Friedrich, O., Erbacher, J., Mutterlose, J., 2006. Paleoenvironmental changes across the Cenomanian/Turonian Boundary Event (Oceanic Anoxic Event 2) as indicated by benthic foraminifera from the Demerara rise (ODP Leg 207). Rev. Micropaleontol. 49, 121–139.
Friedrich, O., Norris, R.D., Erbacher, J., 2012. Evolution of middle to late cretaceous oceans-a 55 m.y. Record of Earth's temperature and carbon cycle. Geology 40, 107–110.
Frijia, G., Forkner, R., Minisini, D., Pacton, M., Struck, U., Mutti, M., 2019. Cyanobacteria proliferation in the cenomanian-turonian boundary interval of the apennine carbonate platform: immediate response to the environmental perturbations associated with OAE-2? geochemistry. Geophys. Geosyst. 20, 2698–2716.
Gale, A.S., Christensen, W.K., 1996. Occurrence of the belemnite Actinocamax plenus in the Cenomanian of SE France and its significance. Bull. Geol. Soc. Denmark 43, 68–77.
Gale, A.S., Jenkyns, H.C., Tsikos, H., van Breugel, Y., Sinninghe Damsté, J.S., Bottini, C., Erba, E., Russo, F., Falzoni, F., Petrizzo, M.R., Dickson, A.J., Wray, D.S., 2019. High-resolution bio- and chemostratigraphy of an expanded record of Oceanic Anoxic Event 2 (Late Cenomanian–Early Turonian) at Clot Chevalier, near Barrême, SE France (Vocontian Basin). Newsletters Stratigr. 52, 97–129.
Gale, A.S., Kennedy, W.J., Voigt, S., Walaszczyk, I., 2005. Stratigraphy of the Upper Cenomanian-lower Turonian Chalk succession at Eastbourne, Sussex, UK: Ammonites, inoceramid bivalves and stable carbon isotopes. Cretac. Res. 26, 460–487.
Gangl, S.K., Moy, C.M., Stirling, C.H., Jenkyns, H.C., Crampton, J.S., Clarkson, M.O., Ohneiser, C., Porcelli, D., 2019. High-resolution records of Oceanic Anoxic Event 2: Insights into the timing, duration and extent of environmental perturbations from the palaeo-South Pacific Ocean. Earth Planet. Sci. Lett. 518, 172–182.
German, C., Holliday, B.P., Elderfield, H., 1991. Redox cycling of rare earth elements in the suboxic zone of the Black Sea. Geochim. Cosmochim. Acta 55, 3553–3558.
German, C.R., Elderfield, H., 1990. Application of the Ce anomaly as a paleoredox indicator: the ground rules. Paleoceanography 5, 823–833.
Goldberg, T., Poulton, S.W., Wagner, T., Kolonic, S.F., Rehkämper, M., 2016. Molybdenum drawdown during cretaceous oceanic anoxic event 2. Earth Planet. Sci. Lett. 440.
Gradstein, F.M., 1992. 43 . Legs 122 and 123 , Northwestern Australian Margin — a Stratigraphic a. Proc. Ocean Drill. Program Sci. Results 123 123, 801–816.
Hancock, J.M., 1975. The petrology of the Chalk. Proc. Geol. Assoc. 86, 499–535.
Haq, B.U., Boyd, R.L., Exon, N.F., von Rad, U., 1992. Evolution of the Central Exmouth Plateau: A Post-Drilling Perspective, in: Proceedings of the Ocean Drilling Program, 122 Scientific Results. Ocean Drilling Program, pp. 801–816.
Haq, B.U., von Rad, U., O'Connell, S., 1991. Shipboard Scientific Party,1990. Site 763., in: Proc. ODP, Init, Repts., 122. College Station, TX (Ocean Drilling Program), pp. 289–352.
Hetzel, A., Böttcher, M.E., Wortmann, U.G., Brumsack, H.-J., 2009. Paleo-redox conditions during OAE 2 reflected in Demerara rise sediment geochemistry (ODP Leg 207). Palaeogeogr. Palaeoclimatol. Palaeoecol. 273, 302–328.
Holmden, C., Jacobson, A.D., Sageman, B.B., Hurtgen, M.T., 2016. Response of the Cr isotope proxy to Cretaceous Ocean Anoxic Event 2 in a pelagic carbonate succession from the Western Interior Seaway. Geochimica et Cosmochimica Acta 186.
Huber, B.T., Norris, R.D., MacLeod, K.G., 2002. Deep-sea paleotemperature record of extreme warmth during the cretaceous. Geology 30, 123–126.
Jenkyns, H.C., 2018. Transient cooling episodes during Cretaceous Oceanic Anoxic Events with special reference to OAE 1a (Early Aptian). Philos. Trans. R. Soc. A Math. Phys. Eng. Sci.
Jenkyns, H.C., 2010. Geochemistry of oceanic anoxic events. Geochem., Geophys. Geosyst. 11, 1–30.
Jenkyns, H.C., Dickson, A.J., Ruhl, M., van den Boorn, S.H.J.M., 2017. Basalt-seawater interaction, the Plenus Cold Event, enhanced weathering and geochemical change: deconstructing Oceanic Anoxic Event 2 (Cenomanian-Turonian, late cretaceous). Sedimentology 64, 16–43.
Jones, C.E., Jenkyns, H.C., 2001. Seawater strontium isotopes, oceanic anoxic events, and seafloor hydrothermal activity in the Jurassic and cretaceous. Am. J. Sci. 301, 112–149.
Kaufman, A.J., Jacobsen, S.B., Knoll, A.H., 1993. The Vendian record of Sr and C isotopic variations in seawater: Implications for tectonics and paleoclimate. Earth Planet. Sci. Lett. 120, 409–430.
Keeling, R.F., Körtzinger, A., Gruber, N., 2010. Ocean Deoxygenation in a Warming World. Ann. Rev. Mar. Sci. 2, 199–229.
Keller, G., Berner, Z., Adatte, T., Stueben, D., 2004. Cenomanian-Turonian and $\delta^{13}C$, and δ18O, sea level and salinity variations at Pueblo, Colorado. Palaeogeogr. Palaeoclimatol. Palaeoecol. 211, 19–43.
Keller, G., Han, Q., Adatte, T., Burns, S.J., 2001. Palaeoenvironment of the Cenomanian–Turonian transition at Eastbourne. England. Cretac. Res. 22, 391–422.
Kerr, A.C., 1998. Oceanic plateau formation: a cause of mass extinction and black shale deposition around the Cenomanian-Turonian boundary? J. Geol. Soc. London 155, 619–626.
Kester, D.R., 1975. Dissolves gases other than CO2, in: Chemical Oceanography. Nature Publishing Group, pp. 497–556.
Kondratiev, S.I., Medvedev, E.V., Konovalov, S.K., 2017. Total Alkalinity and pH in the Black Sea Waters in 2010-2011. Physical Oceanography.
Larson, R.L., 1991. Latest pulse of Earth: evidence for a mid-cretaceous superplume. Geology.
Lawrence, M.G., Greig, A., Collerson, K.D., Kamber, B.S., 2006. Rare earth element and yttrium variability in South East Queensland waterways. Aquat. Geochem. 12, 39–72.
Levin, L.A., 2018. Manifestation, drivers, and emergence of open ocean deoxygenation. Ann. Rev. Mar. Sci. 10, 229–260.
Li, Y.X., Montañez, I.P., Liu, Z., Ma, L., 2017. Astronomical constraints on global carbon-cycle perturbation during Oceanic Anoxic Event 2 (OAE2. Earth Planet. Sci. Lett. 462, 35–46.
Liu, C., Wang, Z., Raub, T.D., 2013. Geochemical constraints on the origin of Marinoan cap dolostones from Nuccaleena Formation, South Australia. Chem. Geol. 351, 95–104.

Liu, X., Byrne, R.H., 1997. Rare earth and yttrium phosphate solubilities in aqueous solution. Geochim. Cosmochim. Acta 61, 1625–1633.
Liu, X.M., Hardisty, D.S., Lyons, T.W., Swart, P.K., 2019. Evaluating the fidelity of the cerium paleoredox tracer during variable carbonate diagenesis on the Great Bahamas Bank. Geochim. Cosmochim. Acta 248, 25–42.
Liu, X.-M., Kah, L., Knoll, A., Cui, H., Wang, C., Bakker, A., Hazen, R.M., 2021. A persistently low level of atmospheric oxygen in Earth's middle age. Nat. Commun. 12, 315.
Lu, Z., Jenkyns, H.C., Rickaby, R.E.M., 2010. Iodine to calcium ratios in marine carbonate as a paleo-redox proxy during oceanic anoxic events. Geology 38, 1107–1110.
Ludden, J.N., Gradstein, F.M., 1990a. Shipboard Scientific Party, 1990. Site 766, in: Proc. ODP, Init. Repts. College Station, TX (Ocean Drilling Program, pp. 269–352.
Ludden, J.N., Gradstein, F.M., 1990b. Shipboard Scientific Party, 1990. Site 765., in: Proc. ODP, Init. Repts. College Station, TX (Ocean Drilling Program), pp. 63–267.
Luo, Y.R., Byrne, R.H., 2004. Carbonate complexation of yttrium and the rare earth elements in natural waters. Geochim. Cosmochim. Acta 68, 691–699.
Martin, E.E., Blair, S.W., Kamenov, G.D., Scher, H.D., Bourbon, E., Basak, C., Newkirk, D. N., 2010. Extraction of Nd isotopes from bulk deep sea sediments for paleoceanographic studies on Cenozoic time scales. Chem. Geol. 269, 414–431.
Montoya-Pino, C., Weyer, S., Anbar, A.D., Pross, J., Oschmann, W., van de Schootbrugge, B., Arz, H.W., 2010. Global enhancement of ocean anoxia during Oceanic Anoxic Event 2: a quantitative approach using U isotopes. Geology 38, 315–318.
Murphy, D.P., Thomas, D.J., 2012. Cretaceous deep-water formation in the Indian sector of the southern Ocean. Paleoceanography 27, 1–12.
Nana, Y.L., Brandon, A.D., Holmden, C., Lau, K.V., Eldrett, J., 2021. Changing inputs of continental and submarine weathering sources of Sr to the oceans during OAE 2. Geochim. Cosmochim. Acta 303, 205–222.
Nakada, R., Tanaka, M., Tanimizu, M., Takahashi, Y., 2017. Aqueous speciation is likely to control the stable isotopic fractionation of cerium at varying pH. Geochim. Cosmochim. Acta 218, 273–290.
Newby, S.M., Young, S.A., Them, T.R., Gill, B.C., Owens, J.D., 2025. Balancing redox budgets: Mechanisms for prolonging anoxia during major carbon burial events. Am. J. Sci. 325. Article 12.
O'Brien, C.L., Robinson, S.A., Pancost, R.D., Sinninghe Damsté, J.S., Schouten, S., Lunt, D.J., Alsenz, H., Bornemann, A., Bottini, C., Brassell, S.C., Farnsworth, A., Forster, A., Huber, B.T., Inglis, G.N., Jenkyns, H.C., Linnert, C., Littler, K., Markwick, P., McAnena, A., Mutterlose, J., Naafs, B.D.A., Püttmann, W., Sluijs, A., van Helmond, N.A.G.M., Vellekoop, J., Wagner, T., Wrobel, N.E., 2017. Cretaceous sea-surface temperature evolution: Constraints from TEX86 and planktonic foraminiferal oxygen isotopes. Earth-Science Rev.
O'Connor, L.K., Jenkyns, H.C., Robinson, S.A., Remmelzwaal, S.R.C., Batenburg, S.J., Parkinson, I.J., Gale, A.S., 2020. A re-evaluation of the Plenus Cold Event, and the links between CO 2 , temperature, and seawater chemistry during OAE 2. Paleoceanogr. Paleoclimatology.
Oschlies, A., Brandt, P., Stramma, L., Schmidtko, S., 2018. Drivers and mechanisms of ocean deoxygenation. Nat. Geosci.
Ostrander, C.M., Owens, J.D., Nielsen, S.G., 2017. Constraining the rate of oceanic deoxygenation leading up to a Cretaceous Oceanic Anoxic Event (OAE-2: ~94 Ma). Sci. Adv. 3, e1701020.
Owens, J.D., Gill, B.C., Jenkyns, H.C., Bates, S.M., Severmann, S., Kuypers, M.M.M., Woodfine, R.G., Lyons, T.W., 2013. Sulfur isotopes track the global extent and dynamics of euxinia during Cretaceous Oceanic Anoxic Event 2. PNAS 110, 18407–18412.
Owens, J.D., Lyons, T.W., Hardisty, D.S., Lowery, C.M., Lu, Z., Lee, B., Jenkyns, H.C., 2017. Patterns of local and global redox variability during the Cenomanian-Turonian Boundary Event (Oceanic Anoxic Event 2) recorded in carbonates and shales from central Italy. Sedimentology 64, 168–185.
Owens, J.D., Lyons, T.W., Hardisty, D.S., Lowery, C.M., Lu, Z., Lee, B., Jenkyns, H.C., 2016a. Patterns of local and global redox variability during the Cenomanian-Turonian Boundary Event (Oceanic Anoxic Event 2) recorded in carbonates and shales from central Italy. Sedimentology 64, 168–185.
Owens, J.D., Lyons, T.W., Li, X., MacLeod, K.G., Gordon, G., Kuypers, M.M.M., Anbar, A., Kuhnt, W., Severmann, S., 2012. Iron isotope and trace metal records of iron cycling in the proto-North Atlantic during the Cenomanian-Turonian oceanic anoxic event (OAE-2). Paleoceanography 27, 1–13.
Owens, J.D., Lyons, T.W., Lowery, C.M., 2018. Quantifying the missing sink for global organic carbon burial during a cretaceous oceanic anoxic event. Earth Planet. Sci. Lett. 499, 83–94.
Owens, J.D., Reinhard, C.T., Rohrssen, M., Love, G.D., Lyons, T.W., 2016b. Empirical links between trace metal cycling and marine microbial ecology during a large perturbation to Earth's carbon cycle. Earth Planet. Sci. Lett. 449, 407–417.
Pancost, R.D., Crawford, N., Magness, S., Turner, A., Jenkyns, H.C., Maxwell, J.R., 2004. Further evidence for the development of photic-zone euxinic conditions during Mesozoic oceanic anoxic events. J. Geol. Soc. London 161, 353–364.
Parente, M., Frijia, G., Di Lucia, M., Jenkyns, H.C., Woodfine, R.G., Baroncini, F., 2008. Stepwise extinction of larger foraminifers at the Cenomanian-Turonian boundary: a shallow-water perspective on nutrient fluctuations during oceanic anoxic event 2 (Bonarelli event). Geology 36, 715–718.
Paul, C.R.C., Lamolda, M.A., Mitchell, S.F., Vaziri, M.R., Gorostidi, A., Marshall, J.D., 1999. The Cenomanian-Turonian boundary at Eastbourne (Sussex, UK): a proposed european reference section. Palaeogeogr. Palaeoclimatol. Palaeoecol. 150, 83–121.
Pearce, M.A., Jarvis, I., Tocher, B.A., 2009. The Cenomanian–Turonian boundary event, OAE2 and palaeoenvironmental change in epicontinental seas: New insights from the dinocyst and geochemical records. Palaeogeogr. Palaeoclimatol. Palaeoecol. 280, 207–234.
Pogge Von Strandmann, P.A.E., Jenkyns, H.C., Woodfine, R.G., 2013. Lithium isotope evidence for enhanced weathering during Oceanic Anoxic Event 2. Nat. Geosci. 6, 668–672.
Robinson, S.A., Murphy, D.P., Vance, D., Thomas, D.J., 2010. Formation of "Southern Component Water" in the late cretaceous: evidence from Nd-isotopes. Geology 38, 871–874.
Robinson, S.A., Dickson, A.J., Pain, A., Jenkyns, H.C., O'Brien, C.L., Farnsworth, A., Lunt, D.J., 2019. Southern Hemisphere sea-surface temperatures during the Cenomanian–Turonian: Implications for the termination of Oceanic Anoxic Event 2. Geology 47, 131–134.
Rue, E.L., Smith, G.J., Cutter, G.A., Bruland, K.W., 1997. The response of trace element redox couples to suboxic conditions in the water column. Deep Res. Part I Oceanogr. Res. Pap. 44, 113–134.
Sageman, B.B., Meyers, S.R., Arthur, M.A., 2006. Orbital time scale and new C-isotope record for Cenomanian-Turonian boundary stratotype. Geology 34, 125.
Scaife, J.D., Ruhl, M., Dickson, A.J., Mather, T.A., Jenkyns, H.C., Percival, L.M.E., Hesselbo, S.P., Cartwright, J., Eldrett, J.S., Bergman, S.C., Minisini, D., 2017. Sedimentary mercury enrichments as a marker for submarine large igneous province volcanism? Evidence from the Mid-Cenomanian Event and Oceanic Anoxic Event 2 (late cretaceous). Geochem. Geophys. Geosyst. 18, 4253–4275.
Schlanger, S.O., Jenkyns, H., 1976. Cretaceous oceanic anoxic events: causes and consequences. Geol. Mijnb. 55, 179–184.
Schlanger, S.O., Arthur, M.A., Jenkyns, H.C., Scholle, P.A., 1987. The Cenomanian-Turonian Oceanic Anoxic Event, I. Stratigraphy and distribution of organic carbon-rich beds and the marine 13C excursion. Geol. Soc. London, Spec. Publ. 26, 371–399.
Schlanger, S.O., Jenkyns, H.C., Premoli-Silva, I., 1981. Volcanism and vertical tectonics in the Pacific Basin related to global cretaceous transgressions. Earth Planet. Sci. Lett. 52, 435–449.
Schmidtko, S., Stramma, L., Visbeck, M., 2017. Decline in global oceanic oxygen content during the past five decades. Nature 542, 335–339.
Scholz, F., Beil, S., Flögel, S., Lehmann, M.F., Holbourn, A., Wallmann, K., Kuhnt, W., 2019. Oxygen minimum zone-type biogeochemical cycling in the Cenomanian-Turonian Proto-North Atlantic across Oceanic Anoxic Event 2. Earth Planet. Sci. Lett. 517, 50–60.
Scotese, C.R., 2004. A continental drift flipbook. J. Geol. 112, 729–741.
Sinton, C.W., Duncan, R.A., 1997. Potential links between ocean plateau volcanism and global ocean anoxia at the Cenomanian-Turonian boundary. Econ. Geol. 92, 836–842.
Slingerland, R., Kump, L.R., Arthur, M.A., Fawcett, P.J., Sageman, B.B., Barron, E.J., 1996. Estuarine circulation in the Turonian Western Interior seaway of North America : Discussion and reply. Gelogical Soc. Am. Bull. 129, 941–952.
Haijun, S., Wignall, P.B., Huyue, S., Dai, X., Chu, D., 2019. Seawater temperature and dissolved oxygen over the past 500 million years. J. Earth Sci. 30, 236–243.
Takashima, R., Nishi, H., Hayashi, K., Okada, H., Kawahata, H., Yamanaka, T., Fernando, A.G., Mampuku, M., 2009. Litho-, bio- and chemostratigraphy across the Cenomanian/Turonian boundary (OAE 2) in the Vocontian Basin of southeastern France. Palaeogeogr. Palaeoclimatol. Palaeoecol. 273, 61–74.
Takashima, R., Nishi, H., Huber, B.T., Leckie, R.M., 2006. Greenhouse would and the Mesozoic Ocean. Oceanography 19, 82–92.
Thomas, D.J., Tilghman, D.S., 2014. Geographically different oceanographic responses to global warming during the Cenomanian-Turonian interval and Oceanic Anoxic Event 2. Palaeogeogr. Palaeoclimatol. Palaeoecol. 411, 136–143.
Tostevin, R., Shields, G.A., Tarbuck, G.M., He, T., Clarkson, M.O., Wood, R.A., 2016. Effective use of cerium anomalies as a redox proxy in carbonate-dominated marine settings. Chem. Geol. 438, 146–162.
Trabucho Alexandre, J., Tuenter, E., Henstra, G.A., Van Der Zwan, K.J., Van De Wal, R.S. W., Dijkstra, H.A., De Boer, P.L., 2010. The mid-cretaceous North Atlantic nutrient trap: Black shales and OAEs. Paleoceanography 25, 1–14.
Tsikos, H., Jenkyns, H.C., Walsworth-Bell, B., Petrizzo, M.R., Forster, A., Kolonic, S., Erba, E., Silva, I.P., Baas, M., Wagner, T., Sinninghe, J.S., 2004. Carbon-isotope stratigraphy recorded by the Cenomanian-Turonian Oceanic Anoxic Event: correlation and implications based on three key localities. J. Geol. Soc. London 162, 576.
Turgeon, S., Brumsack, H.-J., 2006. Anoxic vs dysoxic events reflected in sediment geochemistry during the Cenomanian–Turonian Boundary Event (cretaceous) in the Umbria–Marche Basin of central Italy. Chem. Geol. 234, 321–339.
Turgeon, S.C., Creaser, R.A., 2008. Cretaceous oceanic anoxic event 2 triggered by a massive magmatic episode. Nature 454, 323–326.
van Bentum, E.C., Hetzel, A., Brumsack, H.-J., Forster, A., Reichart, G.-J., Sinninghe Damsté, J.S., 2009. Reconstruction of water column anoxia in the equatorial Atlantic during the Cenomanian–Turonian oceanic anoxic event using biomarker and trace metal proxies. Palaeogeogr. Palaeoclimatol. Palaeoecol. 280, 489–498.
Voigt, S., Gale, A.S., Flögel, S., 2004. Midlatitude shelf seas in the Cenomanian-Turonian greenhouse world: Temperature evolution and North Atlantic circulation. Paleoceanography 19, 1–17.
Webb, G.E., Kamber, B.S., 2000. Rare earth elements in Holocene reefal microbialites: a new shallow seawater proxy. Geochim. Cosmochim. Acta 64, 1557–1565.
Wright, J., Schrader, H., Holser, W.T., 1987. Paleoredox variations in ancient oceans recorded by rare earth elements in fossil apatite. Geochim. Cosmochim. Acta 51, 631–644.
Zhai, R., Zeng, Z., Zhang, R., Yao, W., 2023. The response of nitrogen and sulfur cycles to ocean deoxygenation across the Cenomanian-Turonian boundary. Global Planet. Change 227, 104182.

Zheng, X.-Y., Jenkyns, H.C., Gale, A.S., Ward, D.J., Henderson, G.M., 2013. Changing ocean circulation and hydrothermal inputs during Ocean Anoxic Event 2 (Cenomanian–Turonian): evidence from Nd-isotopes in the European shelf sea. Earth Planet. Sci. Lett. 375, 338–348.

Zhong, S., Mucci, A., 1995. Partitioning of rare earth elements (REEs) between calcite and seawater solutions at 25°C and 1 atm, and high dissolved REE concentrations. Geochim. Cosmochim. Acta 59, 443–453.

Zhou, X., Jenkyns, H.C., Owens, J.D., Junium, C.K., Zheng, X.Y., Sageman, B.B., Hardisty, D.S., Lyons, T.W., Ridgwell, A., Lu, Z., 2015. Upper ocean oxygenation dynamics from I/Ca ratios during the Cenomanian-Turonian OAE 2. Paleoceanography 30, 510–526.